TKK Dissertations 195
Espoo 2009

PREDICTIVE MODELLING OF EDGE TRANSPORT PHENOMENA IN ELMy H-MODE TOKAMAK FUSION PLASMAS

Doctoral Dissertation

Johnny-Stefan Lönnroth

Helsinki University of Technology
Faculty of Information and Natural Sciences
Department of Applied Physics

TKK Dissertations 195
Espoo 2009

PREDICTIVE MODELLING OF EDGE TRANSPORT PHENOMENA IN ELMy H-MODE TOKAMAK FUSION PLASMAS

Doctoral Dissertation

Johnny-Stefan Lönnroth

Dissertation for the degree of Doctor of Science in Technology to be presented with due permission of the Faculty of Information and Natural Sciences for public examination and debate in Auditorium Ko213 at Helsinki University of Technology (Espoo, Finland) on the 1st of December, 2009, at 12 noon.

Helsinki University of Technology
Faculty of Information and Natural Sciences
Department of Applied Physics

Tekniska högskolan
Fakulteten för informations- och naturvetenskaper
Institutionen för teknisk fysik

Distribution:
Helsinki University of Technology
Faculty of Information and Natural Sciences
Department of Applied Physics
P.O. Box 1100
FI - 02015 TKK
FINLAND
URL: http://tfy.tkk.fi/
Tel. +358-9-4511
E-mail: johnny.lonnroth@tkk.fi

ISBN 978-952-248-157-3
ISBN 978-952-248-158-0 (PDF)
ISSN 1795-2239
ISSN 1795-4584 (PDF)
URL: http://lib.tkk.fi/Diss/2009/isbn9789522481580/

TKK-DISS-2670

HSE Print
Helsingfors 2009

ABSTRACT OF DOCTORAL DISSERTATION	HELSINKI UNIVERSITY OF TECHNOLOGY P.O. BOX 1000, FI-02015 TKK http://www.tkk.fi

Author Johnny-Stefan Lönnroth

Name of the dissertation

Predictive modelling of edge transport phenomena in ELMy H-mode tokamak fusion plasmas

Manuscript submitted	27.07.2009	Manuscript revised	26.10.2009
Date of the defence	01.12.2009		
☐ Monograph		X Article dissertation (summary + original articles)	

Faculty	Faculty of Information and Natural Sciences
Department	Department of Applied Physics
Field of research	Plasma physics and fusion energy
Opponent(s)	Prof Dr Arne Kallenbach
Supervisor	Prof Rainer Salomaa
Instructor	Dr Jukka Heikkinen, Dr Taina Kurki-Suonio

Abstract

This thesis discusses a range of work dealing with edge plasma transport in magnetically confined fusion plasmas by means of predictive transport modelling, a technique in which qualitative predictions and explanations are sought by running transport codes equipped with models for plasma transport and other relevant phenomena. The focus is on high confinement mode (H-mode) tokamak plasmas, which feature improved performance thanks to the formation of an edge transport barrier. H-mode plasmas are generally characterized by the occurrence of edge localized modes (ELMs), periodic eruptions of particles and energy, which limit confinement and may turn out to be seriously damaging in future tokamaks.

The thesis introduces schemes and models for qualitative study of the ELM phenomenon in predictive transport modelling. It aims to shed new light on the dynamics of ELMs using these models. It tries to explain various experimental observations related to the performance and ELM-behaviour of H-mode plasmas. Finally, it also tries to establish more generally the potential effects of ripple-induced thermal ion losses on H-mode plasma performance and ELMs.

It is demonstrated that the proposed ELM modelling schemes can qualitatively reproduce the experimental dynamics of a number of ELM regimes. Using a theory-motivated ELM model based on a linear instability model, the dynamics of combined ballooning-peeling mode ELMs is studied. It is shown that the ELMs are most often triggered by a ballooning mode instability, which renders the plasma peeling mode unstable, causing the ELM to continue in a peeling mode phase. Understanding the dynamics of ELMs will be a key issue when it comes to controlling and mitigating the ELMs in future large tokamaks. By means of integrated modelling, it is shown that an experimentally observed increase in the ELM frequency and deterioration of plasma confinement triggered by external neutral gas puffing might be due to a transition from the second to the first ballooning stable region in magnetohydrodynamics (MHD). The result may have implications on the control of ELMs and performance in future tokamaks. Modest pedestal performance and benign ELMs observed in the presence of toroidal magnetic field ripple in dimensionless pedestal identity experiments between the JET and JT-60U tokamaks are explained through predictive transport modelling as resulting from ripple-induced thermal ion losses, non-diffusive (direct) losses to be specific. It is shown that ripple losses need not necessarily have a detrimental influence on performance, but that there is a trade-off between performance and benignity of ELMs. The results may have widely felt implications, because ITER, the next major facility on the way towards a commercial fusion reactor, is foreseen to operate with a non-negligible level of toroidal magnetic field ripple.

Keywords	fusion, tokamak, transport, modelling, H-mode, ELM, magnetic ripple		
ISBN (printed)	978-952-248-157-3	ISSN (printed)	1795-2239
ISBN (pdf)	978-952-248-158-0	ISSN (pdf)	1795-4584
Language	English	Number of pages	77 + app. 123
Publisher	Department of Applied Physics, Helsinki University of Technology		
Print distribution	Department of Applied Physics, Helsinki University of Technology		

X The dissertation can be read at http://lib.tkk.fi/Diss/2009/isbn9789522481580/

SAMMANFATTNING (ABSTRAKT) AV DOKTORSAVHANDLING	TEKNISKA HÖGSKOLAN PB 1000, FI-02015 TKK http://www.tkk.fi

Författare Johnny-Stefan Lönnroth

Titel

Predictive modelling of edge transport phenomena in ELMy H-mode tokamak fusion plasmas

Inlämningsdatum för manuskript 27.07.2009	Datum för disputation 01.12.2009
Datum för det korrigerade manuskriptet 26.10.2009	
☐ Monografi	X Sammanläggningsavhandling (sammandrag + separata publikationer)

Fakultet	Fakulteten för informations- och naturvetenskaper
Institution	Institutionen för teknisk fysik
Forskningsområde	Plasmafysik och fusionsenergi
Opponent(er)	Prof. Dr Arne Kallenbach
Övervakare	Prof. Rainer Salomaa
Handledare	TkD Jukka Heikkinen, PhD Taina Kurki-Suonio

Sammanfattning (Abstrakt)

Denna avhandling behandlar en serie studier, i vilka transport i randzonen i magnetiskt sammanhållna fusionsplasmor har analyserats genom prediktiv transportmodellering. Ifrågavarande teknik går ut på att man genom att köra numeriska transportkoder kvalitativt försöker förklara och förutspå olika fysikaliska fenomen. Fokus i denna avhandling ligger på H-modplasmor i tokamakreaktorer, det vill säga plasmor som har hög inneslutning tack vare att en transportbarriär har bildats i randplasman. Karakteristiskt för H-modplasmor är förekomsten av ELMs (edge localized modes), en typ av periodiska eruptioner av energi och partiklar från randplasman, vilka begränsar inneslutningen och kan skada reaktorväggarna i framtida stora tokamakreaktorer.

I avhandlingen föreslås nya modeller och tekniker för att kvalitativt studera ELM-eruptioner i prediktiva transportsimulationer. ELM-fenomenets dynamik studeras. Förklaringar söks till diverse experimentella observationer gällande inneslutningen och ELM-egenskaperna i H-modplasmor. Effekterna av rippelförluster av termiska joner på H-modplasmors prestanda och ELM-eruptioner utforskas.

Det visas att de i avhandlingen presenterade ELM-modellerna kvalitativt kan reproducera olika ELM-regimers experimentella dynamik. Dynamiken av ELM-eruptioner drivna av en kombination av magnetohydrodynamiska (MHD) instabiliteter av både ballooning- och peeling-typ studeras med en teoribaserad linjär ELM-modell. Det visas att ELM-eruptioner oftast utlöses av instabiliteter av ballooning-typ, vars inverkan på plasman sedan får densamma att bli peeling-instabil, varvid eruptionen fortsätter i en peeling-fas. Dylika insikter i ELM-dynamik kan ha stor betydelse, när det gäller att kontrollera och förmildra ELM-eruptionerna i framtida tokamakreaktorer. Med hjäp av integrerad simulering visas det att den försämrade prestanda i kombination med en förhöjd ELM-frekvens, som ofta observeras vid förhöjd extern neutralgasinjicering, kan tänkas bero på en transition från det andra till det första stabilitetsområdet inom MHD. Resultatet kan ha implikationer för ELM-kontroll i framtida tokamakreaktorer. Prediktiv simulering visar också att nedsatt prestanda och mindre ELM-eruptioner under inflytande av toroidalt magnetfältsrippel i identitetsexperiment mellan tokamakanläggningarna JET och JT-60U kan tänkas bero på rippelinducerade direkta (icke-diffusiva) förluster av termiska joner. Det visas dessutom att rippelförluster inte nödvändigtvis behöver ha en nedsättande inverkan på prestandan, utan att nedsatt prestanda bara korrelerar med små ELM-eruptioner och vice versa. Dessa resultat kan ha långtgående konsekvenser, emedan ITER, följande anläggning på vägen mot ett kommersiellt fusionskraftverk, är tänkt att fungera med en icke-försumbar nivå av toroidalt magnetiskt rippel.

Ämnesord (Nyckelord)	fusion, tokamak, transport, modellering, H-mod, ELM, magnetfältsrippel		
ISBN (tryckt)	978-952-248-157-3	ISSN (tryckt)	1795-2239
ISBN (pdf)	978-952-248-158-0	ISSN (pdf)	1795-4584
Språk	Engelska	Sidantal	77 + bil. 123
Utgivare	Institutionen för teknisk fysik, Tekniska högskolan		
Distribution av tryckt avhandling	Institutionen för teknisk fysik, Tekniska högskolan		
X Avhandlingen är tillgänglig på nätet http://lib.tkk.fi/Diss/ 2009/isbn9789522481580/			

Abstract

This thesis discusses a range of work dealing with edge plasma transport in magnetically confined fusion plasmas by means of predictive transport modelling, a technique in which qualitative predictions and explanations are sought by running transport codes equipped with models for plasma transport and other relevant phenomena. The focus is on high confinement mode (H-mode) tokamak plasmas, which feature improved performance thanks to the formation of an edge transport barrier. H-mode plasmas are generally characterized by the occurrence of edge localized modes (ELMs), periodic eruptions of particles and energy, which limit confinement and may turn out to be seriously damaging in future large tokamak reactors.

The thesis introduces schemes and models for qualitative study of the ELM phenomenon in predictive transport modelling. It aims to shed new light on the dynamics of ELMs using these models. It tries, again making use of the ELM modelling schemes, to explain various experimental observations, notably the loss of performance and increased ELM frequency observed in experiments with enhanced toroidal magnetic field ripple and in situations with strong external neutral gas puffing. Finally, it also tries to establish more generally the potential effects of ripple-induced thermal ion losses on H-mode plasma performance and ELMs.

It is demonstrated that the ELM modelling schemes introduced in the thesis can qualitatively reproduce the experimental dynamics of a number of ELM regimes. Using a theory-motivated ELM model based on a linear model of instability, the dynamics of combined ballooning-peeling mode ELMs is studied. It is shown that the ELMs are most often triggered by a ballooning mode instability, which renders the plasma peeling mode unstable and causes the ELM to continue in a peeling mode phase. Understanding the dynamics of ELMs will be a key issue when it comes to controlling and mitigating the ELMs in future large tokamaks. By means of integrated modelling, it is shown that an experimentally observed increase in the ELM frequency and deterioration of plasma confinement triggered by external neutral gas puffing might be due to a transition from the second to the first ballooning stable region, as expressed in magnetohydrodynamics (MHD). The result may have implications on the control of ELMs and performance in future tokamaks. Modest pedestal performance and benign ELMs observed in the presence of toroidal magnetic field ripple in dimensionless pedestal identity experiments between the JET and JT-60U tokamaks are explained through predictive transport modelling as resulting from ripple-induced thermal ion losses, more precisely from non-diffusive (direct) losses. It is shown that ripple losses need not necessarily have a detrimental influence on performance, but that there is a trade-off between performance and benignity of ELMs. The results may have widely felt implications, because ITER, the next major facility on the way towards a commercial fusion reactor, is foreseen to operate with a non-negligible level of toroidal magnetic field ripple.

Preface

The research presented in this thesis has been carried out at EFDA-JET (the Joint European Torus (JET) under the auspices of the European Fusion Development Agreement (EFDA)) in Culham, United Kingdom since early 2002 on a series of secondments from Helsinki University of Technology in Esbo, Finland. I have been fortunate enough to carry out my work at one of the leading magnetic fusion laboratories in the world. It has been a challenging journey into the realm of nuclear fusion research, during which I have managed both to endeavour professionally and to make acquaintances and build friendships.

Successfully pursuing the research resulting in this thesis would not have been possible without the help of a great many people. Most of all I am indebted to my long-time supervisor at JET, Dr Vassili Parail, without whose thorough guidance, helpful insights and unrivalled experience the work would have been overwhelmingly harder to pursue. It has been a pleasure and a privilege to work with him. I would also like to thank the other members of the Code Management Group at JET for their contributions. Similarly, I would like to acknowledge the contributions of many other colleagues at JET and around the world, whom I have collaborated with. I am also grateful to the leaders of Task Force Transport at JET for providing me the formal framework for doing science at JET.

Closer to home, I would like to thank Professor Rainer Salomaa and Dr Seppo Karttunen for first giving me the opportunity to work within the Finnish fusion research association and then nominating me for a series of secondments to JET. A special thanks also belongs to Dr Taina Kurki-Suonio for carefully reading the manuscript and giving numerous suggestions for improvements to the text.

Last but not least, I want to express my gratitude to all those who have supported me on a more personal level during the years of my thesis research. I especially want to thank my parents for their hospitality during my numerous trips to my native Finland and the whole family including my three siblings for their companionship. My many friends in the United Kingdom deserve a special thanks for their friendship and fellowship. Likewise, I would like acknowledge my many friends in Finland for staying in touch and regularly meeting up with me despite my many years abroad.

The work in this thesis, supported by the European Communities under the contract of Association between Euratom / Tekes, has been carried out within the framework of the European Fusion Development Agreement. The views and opinions expressed herein do not necessarily reflect those of the European Commission.

Financial support from the Fortum Foundation is gratefully acknowledged.

Culham, United Kingdom; 19 May 2009
Johnny Lönnroth

List of Appended Publications

This thesis is a review and discussion of the main results reported in the following original publications:

1. J.-S. Lönnroth, V.V. Parail, G. Corrigan, D. Heading, G. Huysmans, A. Loarte, S. Saarelma G. Saibene, S. Sharapov, J. Spence, *"Integrated predictive modelling of the effect of neutral gas puffing in ELMy H-mode plasmas"*, Plasma Physics and Controlled Fusion **45** 1689-1711 (2003).

2. J.-S. Lönnroth, V. Parail, G. Huysmans, G. Saibene, H. Wilson, S. Sharapov, G. Corrigan, D. Heading, R. Sartori, M. Bécoulet, *"Predictive transport modelling and MHD stability analysis of mixed type I-II ELMy H-mode JET plasmas"*, Plasma Physics and Controlled Fusion **46** 767-796 (2004).

3. J.-S. Lönnroth, V. Parail, C. Figarella, X. Garbet, G. Corrigan, D. Heading, *"Predictive modelling of ELMy H-modes with a new theory-motivated model for ELMs"*, Plasma Physics and Controlled Fusion **46** A249-A256 (2004).

4. J.-S. Lönnroth, V. Parail, A. Dnestrovskij, C. Figarella, X. Garbet, H. Wilson, *"Predictive transport modelling of type I ELMy H-mode dynamics using a theory-motivated combined ballooning-peeling model"*, Plasma Physics and Controlled Fusion **46** 1197-1215 (2004).

5. J.-S. Lönnroth, V. Parail, V. Hynönen, T. Johnson, T. Kiviniemi, N. Oyama, M. Beurskens, D. Howell, G. Saibene, P. de Vries, T. Hatae, Y. Kamada, S. Konovalov, A. Loarte, K. Shinohara, K. Tobita, H. Urano, *"Effects of ripple-induced ion thermal transport on H-mode plasma performance"*, Plasma Physics and Controlled Fusion **49** 273-295 (2007).

6. J.-S. Lönnroth, G. Corrigan, W. Fundamenski, V. Parail, J. Spence, D. Tskhakaya, *"Analysis of ELM heat pulse propagation in the JET scrape-off layer with an integrated fluid-kinetic approach"*, Europhysics Conference Abstracts **29C** P-4.040 (2005).

The author of the thesis is the principal author of all the aforementioned publications and has actively participated in all the work reported in them. He has carried out all the simulations and all the analysis reported upon in the publications, with the exception of the orbit-following simulations with the numerical code ASCOT discussed in Publication 5.

Contents

Chapter 1

Introduction

1.1 Plasma Confinement for Nuclear Fusion

Utilizing thermonuclear fusion for large-scale electricity generation would feature significant environmental and other advantages, making it too promising a concept not to be explored [1, 2]. Traditionally, fusion energy research has been pursued along two diametrically opposite plasma confinement strategies, customarily referred to as inertial confinement fusion [3] and magnetic confinement fusion [4], the latter of which appears to have been developed further along what has over the years turned out to be an increasingly tortuous path towards commercial application. The idea in inertial confinement fusion is to periodically compress and ignite small fuel pellets of deuterium and tritium by intense laser beams, thereby intermittently igniting fusion reactions delivering massive bursts of energy. In magnetic confinement fusion, the endeavour is to keep the fusion plasma, foreseen to be a mixture of deuterium and tritium in the first generation of fusion reactors, confined in a magnetic field and heat it up sufficiently for a sustained fusion burn to occur.

In order to achieve thermonuclear fusion conditions in a fusion reactor operating according to the magnetic confinement concept, it is necessary to confine the fusion plasma for a sufficiently long time. Various confinement concepts have been devised, with the more successful ones all having in common that they make use of toroidal geometry. In a toroidal device, a toroidal magnetic field alone is insufficient to provide confinement of the plasma. In order to prevent polarization of the plasma by drifting particles, the magnetic field lines need to be helically twisted, i.e. the field needs a poloidal component.

In a tokamak [5, 6], the toroidal field is generated by a toroidal field coil system surrounding the plasma, whereas the poloidal field is created by driving a current

through the plasma. Traditionally, most of the current is driven inductively, so that the plasma operates as the secondary circuit of a transformer. When a current starts to flow in the primary circuit, it induces an electric field in the plasma, which drives the toroidal plasma current. The inductive current is referred to as Ohmic current.

Already in the early days of fusion research, it was shown that the level of performance, under certain assumptions, is proportional to the value of the triple product $n_e \tau_E T$, where n_e is the (electron) density, τ_E is the energy confinement time, i.e. the characteristic time it takes for the plasma to lose through various physical processes an amount of energy corresponding to its stored thermal energy, and T is the temperature [7]. Because the required high temperature cannot be reached by Ohmic heating alone, various auxiliary heating schemes are generally employed, such as the injection of energetic neutral particle beams into the plasma, a technique known as neutral beam injection (NBI) heating [8, 9], and absorption of radio frequency waves at plasma resonances, a scheme referred to as radio frequency (RF) heating [10].

A high plasma temperature is a prerequisite also for the simple reason that a substantial enough fraction of the plasma ions needs to have high enough energies to overcome the Coulomb potential barrier between the nuclei, i.e. charges of the same sign, and thereby make fusion reactions happen. Ignition, i.e. a completely self-sustained burn without the application of external heating, is, for various reasons, not necessarily even desirable, but the plasma needs to be heated to a regime where the relevant fusion cross section is large enough for a substantial net energy gain to be obtained.

Diffusion, convection and radiation losses limit confinement by affecting the energy confinement time, whereas increasing the magnetic field or the size of the tokamak improves it. There are stringent physical limits on the magnetic field strength applicable in a tokamak, and it is costly to increase the size of the device. Therefore, it is the physics behind the tendency of heat and particles to move away from the centre of the plasma that needs to be understood and controlled. Particle and heat transport, as the subject is known as, has become a key research area within the field of magnetic confinement fusion.

1.2 Basics of Plasma Transport

Despite immense efforts, many features of plasma transport are still not theoretically understood. In all tokamaks, the measured heat and particle diffusivities exceed the predictions of collisional transport theory substantially. There are strong indications, supported by turbulence measurements in experiments, that the in-

creased transport, referred to as anomalous transport, is due to plasma micro-turbulence [12].

Transport in tokamak plasmas is normally dominated by diffusive processes. In classical transport theory, transport arises from Coulomb collisions between the particles. The random walk model provides the simplest approach for calculating the diffusion coefficients. The level of diffusion obtained by random walk arguments in a cylindrical plasma is referred to as classical transport. [13, 14]

In a real tokamak plasma, the calculation is far more complex. There are large numbers of electrons and ions colliding with each other, which results in different types of transport and losses. These have to be taken into account. Furthermore, significant additional transport arises owing to the toroidal geometry. The most important contribution derives from the fact that, unlike in cylindrical geometry, the parallel and perpendicular dynamics are coupled. The viscosity in toroidal geometry also leads to additional transport. The transport calculated in this way for a torus, in which the magnetic field lines are curved, is referred to as neo-classical transport [15].

Experimentally measured transport in tokamaks typically exceeds the neo-classically predicted level by at least an order of magnitude. Much effort has been put into the study of anomalous transport and the micro-turbulence in the electric and magnetic fields believed to be the cause of it [16]. The present understanding is that it is the free energy sources of the micro-instabilities, essentially the density and temperature gradients, that drive the turbulent transport [16, 17]. In the plasma core, these micro-instabilities can roughly be classified according to their source of free energy into modes driven by the ion temperature gradient, by the electron temperature gradient and by the pressure gradient.

1.3 Magnetohydrodynamic Stability

In many cases, a plasma can be treated as a fluid and its stability analysed by means of magnetohydrodynamics (MHD), a discipline of physics concerned with the dynamics of electrically conducting fluids. MHD builds on the well-established phenomenology that magnetic fields can induce currents in a moving conductive fluid and that these currents then create forces on the fluid and also change the magnetic field itself. Mathematically, MHD can be described by a combination of sets of equations known as the Navier-Stokes equations for fluid dynamics and Maxwell's equations of electromagnetism [18]. The fact that MHD is a fluid theory, i.e. it treats the plasma as a fluid without looking at the individual particles in it and their interactions, means that it cannot treat kinetic phenomena, i.e. those in

which the existence of discrete particles or of a non-thermal velocity distribution are important.

It is customary to distinguish between linear and non-linear MHD and ideal and resistive MHD. Linear MHD is a simplification based on linear approximations of the full MHD equations. Ideal MHD assumes that the fluid has so little resistivity that it can be treated as a perfect conductor, whereas resistive MHD takes plasma resistivity into account. Ideal MHD is strictly only applicable when the plasma is strongly collisional, so that the time scale of collisions is shorter than the other characteristic times in the system, and the particle distributions are Maxwellian.

MHD is a discipline intrinsically related to plasma stability and thereby to the performance of fusion plasmas. This causality derives from the fact that there are numerous instabilities of a magnetohydrodynamic nature that limit plasma confinement and in some cases may cause a disruption, a sudden loss of thermal energy often followed by termination of the plasma discharge. For instance, one of the critical stability issues for magnetic fusion is that MHD instabilities tend to limit plasma performance at high β, where β is a measure of plasma pressure normalized to the magnetic field strength, a high value of which is often seen as crucial for a compact, cost-effective magnetic fusion reactor. The next subsection will specifically focus on a phenomenon known as edge-localized modes, thought to be driven by MHD instabilities, which is generally seen as one of the main obstacles in the quest for viable commercial application of fusion energy.

MHD instabilities are generally described according to their toroidal n and poloidal m mode numbers. The mode number is a measure of the number of wavelengths the mode forms along the circumference of the plasma, in the toroidal or poloidal direction depending on whether one talks about the toroidal or poloidal mode number, respectively. Two types of instabilities, in particular, are important in the edge plasma. Modes with low toroidal mode numbers, generally in the range $n \lesssim 10$, are to a large extent driven by the edge current and are known as kink or peeling modes. Modes with higher toroidal mode numbers, say $n \gtrsim 10$, on the other hand, are mostly controlled by the edge pressure gradient and are known as ballooning modes. [19, 20]

1.4 ELMy H-Mode Plasmas

Finding ways of reducing the level of anomalous transport in order to improve plasma confinement has been a key research area for many years. Dramatic progress in this area has also been made. Most importantly, the so-called high confinement mode (H-mode) was discovered in the ASDEX tokamak in 1982 [21]. The H-mode is

characterized by a suppression of turbulent transport in a narrow layer just inside the last closed flux surface or separatrix, which defines the boundary of the confined plasma. This layer with improved transport characteristics is referred to as the edge transport barrier (ETB) or H-mode pedestal. Thanks to the reduced, roughly ion neo-classical, level of transport in the ETB, this region develops a steeper pressure gradient than the plasma deeper in the core. Owing to a phenomenon known as profile stiffness [22–29], a well-known tendency of the relative temperature gradient to remain insensitive to variations in the boundary conditions over large plasma regions, the pressure profile in the core maintains roughly the same gradient as it would in the absence of an ETB. Hence, the thermal energy content of the plasma, and thus confinement, is considerably higher in the H-mode than in the reference situation without an ETB known as the low confinement mode (L-mode). H-mode plasmas typically feature a level of confinement $2-3$ times better than corresponding L-mode plasmas.

Figure 1.1 illustrates the improvement in plasma pressure achieved in the H-mode. The figure shows a typical pressure profile in an L-mode plasma and what this profile would change into after a transition to the H-mode. The region with the steep pressure gradient just inside the separatrix in the H-mode pressure profile is the ETB. The figure clearly illustrates that the ETB is the source of the overall improved performance in the H-mode, given that the L-mode and the H-mode maintain the same pressure gradient in the rest of the plasma.

The H-mode ubiquitously features periodic bursts of energy and particles from the ETB into the so-called scrape-off layer (SOL), i.e. the region with open flux surfaces outside the separatrix. These eruptions accompanying the H-mode are known as edge localized modes (ELMs) and, for several reasons, play a key role in determining the performance of tokamaks. To begin with, the occurrence of the ELM instability severely limits the achievable pressure gradient in the ETB and ,thus, also overall plasma confinement. Secondly, ELMs cause severe peak heat loads on the divertor target plates, to which the heat and particle flows of the SOL are channelled. Coping with these heat loads is foreseen to be a major challenge in the design of future tokamak reactors. ELMs, however, also have beneficial effects on plasma performance. In particular, ELMs help to transport impurity ions across the pedestal region out of the confined plasma. ELM-free plasmas usually terminate due to accumulation of impurities, because particles and especially impurities are rather well confined in them. Impurities in fusion plasmas originate from plasma-wall interactions with the vacuum vessel walls and, in the form of helium ash, from the fusion reaction. Because impurity accumulation is a bigger or lesser problem in all tokamak plasmas, impurity transport has turned into a major research area.

ELMs are broadly believed to be driven by MHD instabilities in the edge plasma. A commonly held view is that ELM stability is controlled by a combination of ballooning and peeling modes and their interaction [30–39].

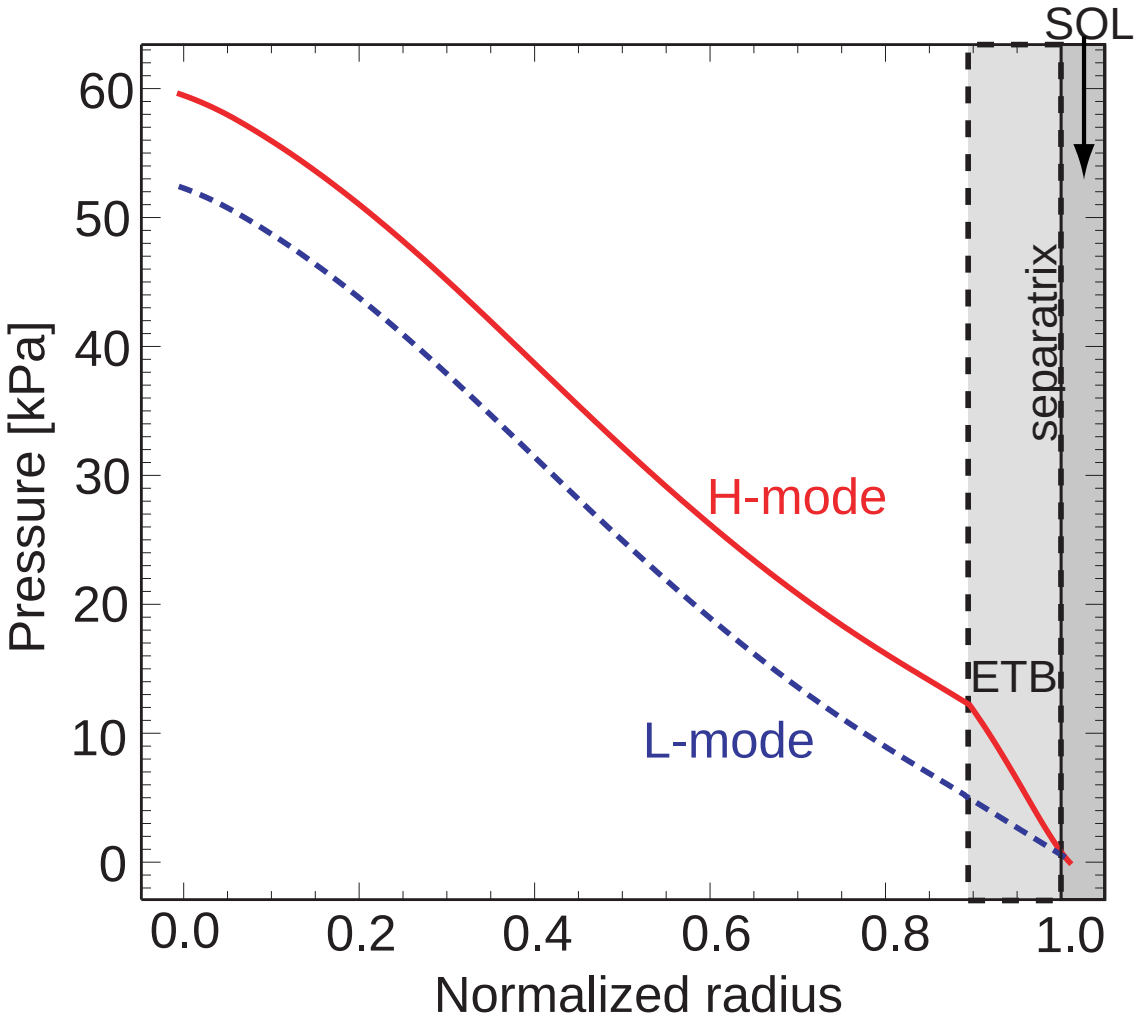

Figure 1.1: *Typical pressure profile in an L-mode plasma (dashed curve) and the corresponding pressure profile after a transition into H-mode (full line).*

Various ELM regimes have been identified. Type I or "giant" ELMs are the most commonly observed type of ELMs in plasmas with large enough heating power. They are large events capable of removing up to 10% of the plasma energy and feature a repetition frequency that increases with increasing heating power. Typically, the ELM frequency in operation with type I ELMs, or what is referred to as type I ELMy H-mode, is of the order of tens of hertz. Type III ELMs are small and very frequent, and are often seen slightly above the H-mode threshold power, i.e. the heating power necessary to establish an H-mode. Type II ELMs resemble type III ELMs, but are generally even tinier and more frequent. Sometimes MHD activity in type II ELMy H-mode has a continuous rather than an intermittent character. Type III ELMs are generally characterized by an ELM frequency that decreases with power [40]. Another distinction between ELM types II and III, both of which are commonly referred to as "grassy ELMs", is based on their different effects on plasma

performance. Generally, type II ELMs do not lead to a serious reduction in plasma confinement, whereas type III ELMs are associated with a significant deterioration of plasma confinement, compared to operation with type I ELMs. Type II ELMs often occur in a mixed type I-II ELMy H-mode regime, i.e. in a mode of operation with tiny, frequent type II ELMs interrupted by occasional large type I ELMs. [41, 42]

Type I ELMy H-mode is the most thoroughly investigated tokamak scenario. Given that type I ELMy H-mode is a robust mode of operation seen in a variety of conditions in a large number of tokamaks and features good confinement properties, it has been chosen as the reference operational scenario for the International Thermonuclear Experimental Reactor (ITER) [43–45], the next big fusion experiment to be contemplated by the international community. Type I ELMy H-mode is, however, associated with certain disadvantages from the point of view of operation of a real power plant. Firstly, ELM mitigation will be needed already in ITER due to the large peak divertor heat loads associated with type I ELMs. Accordingly, much effort has already been put into developing alternative H-mode scenarios with less violent ELMs. Secondly, a large fraction of the plasma current is driven inductively in the H-mode. This is a disadvantage, because it leads to pulsed operation, which is not desirable in the case of a power plant. The pulsed operation follows from the requirement of transformer action to drive the plasma current.

In the end, the "ELMy H-mode Scenario" or "Conventional Tokamak Scenario", as it often referred to as, might not be a feasible mode of operation for a commercial fusion reactor owing to the limitation of pulsed operation. In order to render the tokamak concept compatible with continuous operation, development has started on so-called "Advanced Tokamak Scenarios" [46], in which a large fraction of the plasma current is driven non-inductively as a diffusion-driven current known as the bootstrap current [6]. Other goals in advanced scenario development is to increase the margins at a given reactor size, i.e. make the viable reactor size smaller, to increase the fusion power density and to increase confinement by means of internal transport barriers. The primary means to achieve the goals in advanced scenario development is to optimize the shape of the current density and pressure profiles by external current drive and heating as well as by the optimal alignment of the bootstrap current.

Given the robustness of the H-mode, it is clear, however, that it will remain a reference mode of operation for the foreseeable future, as the fusion community pools its resources towards ITER. Consequently, improving the understanding of the ELM phenomenon, learning how to mitigate ELMs and developing alternative ELMy H-mode scenarios, i.e. regimes with less violent ELMs, remain high-priority research areas.

1.5 Transport in the Scrape-off Layer

In the SOL, perpendicular transport across the magnetic field is balanced by parallel flow along the open field lines towards the divertor target plates. The perpendicular transport across the field lines is generally larger than that predicted by neo-classical theory. It can be shown that in steady-state, when there are no sources or sinks in the SOL and the losses along the field is balanced by the net flow across the field into the flux tube, the density and temperature profiles decay exponentially when moving outward from the separatrix [6].

For parallel transport along the field lines in the SOL there are various models, both kinetic models and fluid models [47]. The kinetic description is the most fundamental way to describe a plasma. In the kinetic approach, a distribution function $f(\vec{x}, \vec{v}, t)$ for the positions $\vec{x}$ and velocities $\vec{v}$ of the particles is obtained by solving an equation known as the Boltzmann equation or reduced forms thereof [47]. The fluid description, which seeks to reduce the complexities of the kinetic description, describes the plasma in terms of macroscopic quantities such as density, mean velocity, and mean energy obtained by taking moments of the distribution function. The equations for macroscopic quantities, called fluid equations, are obtained by taking velocity moments of the Boltzmann equation.

Generally, parallel flow along the field lines is much faster faster than perpendicular flow across the field lines. The perpendicular fluid velocity $v_\perp$ may be as low as 1 m/s, whereas the parallel velocity is roughly equal to the plasma sound speed $c_s = [(T_e + T_i)/m_i]^{1/2}$, which is typically several orders of magnitude larger. Here, T_e is the electron temperature, T_i is the ion temperature and m_i the ion mass.

1.6 Ripple Transport

It has been noted that the small periodic variation of the toroidal magnetic field in a tokamak due to the discreteness introduced by the system of toroidal field coils can give rise to small levels of additional ion thermal transport owing to a number of mechanisms. The level of additional transport, referred to as ripple transport, is expected to be small and can safely be considered negligible inside the ETB. Within the ETB, however, where the level of residual transport is small, ripple-induced transport may have palpable effects.

The finite number of toroidal field coils in a tokamak leads to a systematic variation of the magnetic field strength. The coils produce a short-wavelength ripple in the magnetic field strength as a field line is traced around the torus. For N toroidal

field coils, in the case of circular symmetry and a large-aspect-ratio tokamak, the magnetic field can be approximated by

$$B = B_0(1 - \epsilon\cos\theta)(1 - \delta(r,\theta)\cos(N\phi)), \tag{1.1}$$

where θ is the poloidal angle, ϕ is the toroidal angle, ϵ is the inverse aspect ratio of the tokamak and $\delta(r,\theta)$ is the level of ripple, determined by the coil configuration.

Figure 1.2 provides graphical illustrations of the spatial variation of the magnetic field strength in a tokamak. Both plots in the figure have been drawn using data from the plasma configuration foreseen for the ITER tokamak for a location near the separatrix. Frame (a) shows the variation of the magnetic field strength as a function of the poloidal and toroidal angles. The variation over a full poloidal revolution follows from the variation of the local major radius over the poloidal revolution. In a tokamak, the magnetic field strength can be shown to be inversely proportional to the local major radius. The periodic variation of the magnetic field strength as a function of the toroidal angle follows from the discreteness of the toroidal magnetic field coil configuration. This scant inhomogeneity of the field in the toroidal direction is what is referred to as toroidal magnetic field ripple. Drawn in figure is also a magnetic field line, the helical path of which takes it across the parameter space several times. Following the field line in the plot gives an impression of how the magnetic field strength varies along it as it traces its way around the torus. Frame (b) provides an illustration of how the level of ripple varies in the poloidal plane. The ripple amplitude decreases rapidly, when moving from the edge towards the centre of the plasma.

An important consequence of the rippled structure of the magnetic field is the creation of magnetic wells and particle trapping associated with these wells. It can be shown that the wells vanish for $\epsilon/Nq\delta\sin\theta > 1$ [48]. The condition divides the plasma cross-section into two regions: a ripple well region in which toroidal ripple wells exist and region without wells. Here, q is the safety factor, a parameter measuring the number of toroidal revolutions around the torus for each poloidal revolution of a field line. The safety factor plays an important role in determining the stability of tokamak plasmas.

Transport in both regions is affected by the ripple, but in different ways. In the ripple well region, the most important effect is particle trapping, i.e. particles becoming trapped in the local toroidal wells and subsequently lost from the plasma via the so-called gradient drift [6] due to the gradient of the magnetic field. In the remainder of the plasma, the ripple modifies particle orbits, thus leading to transport. The ripple in particular affects the so-called banana trapped particles, a class of particles belonging to the low-collisionality, so-called banana regime, in which transport scales linearly with the collision frequency [48].

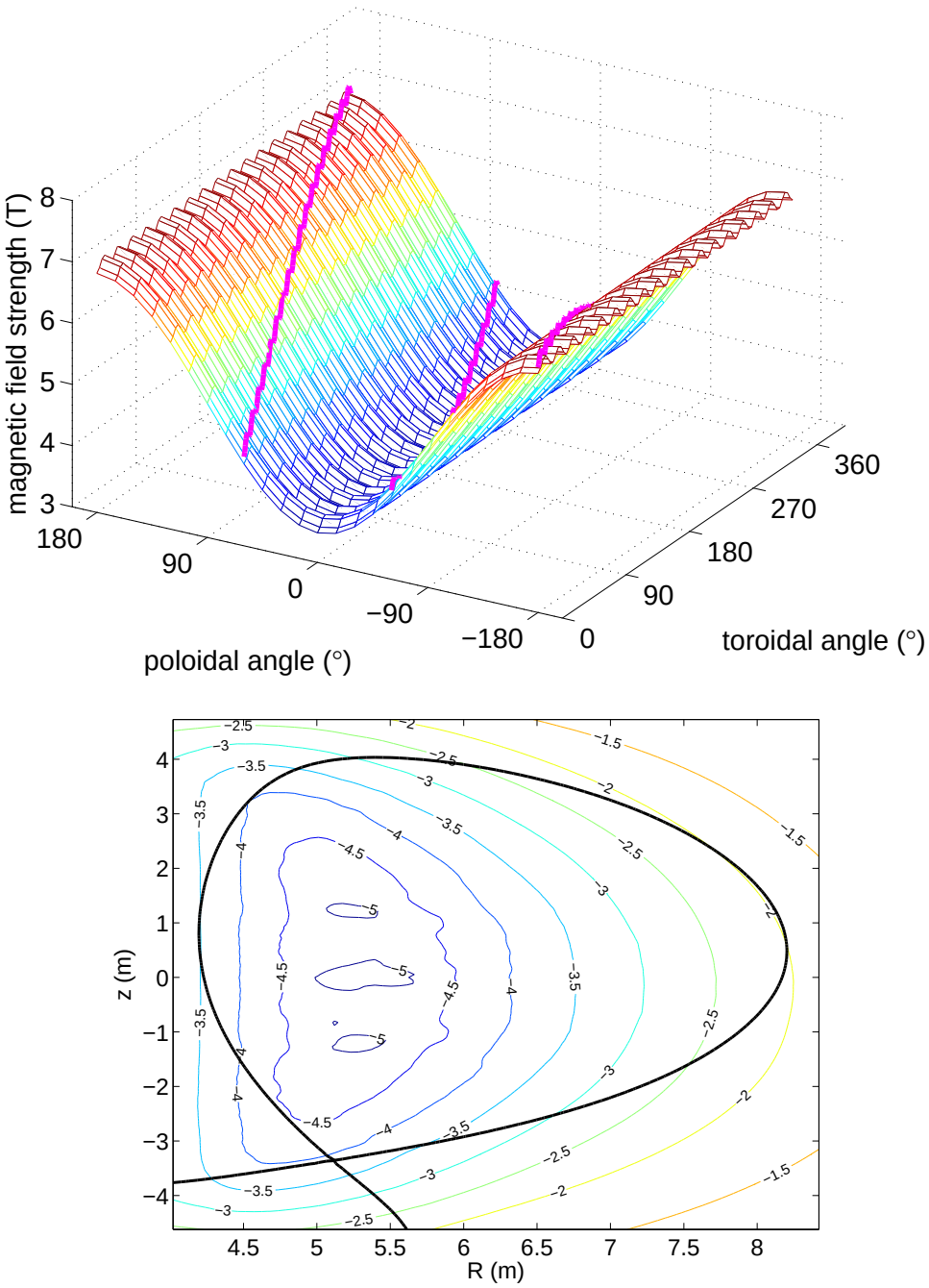

Figure 1.2: *(a) The magnetic field strength at a location near the separatrix in ITER as a function of the poloidal and toroidal angles. The magenta trace (which enters and exits the plot area several times) is a magnetic field line. (b) A ripple map with contours indicating locations with equal ripple. The number associated with each contour, defined as* $\log_{10}\delta$*, gives the ripple amplitude. The thick black curve denotes the location of the separatrix. Figures courtesy of Tuomas Koskela, Laboratory of Advanced Energy Systems Helsinki University of Technology.*

Ripple well and ripple banana transport affect both thermal plasma particles and highly energetic particles such as neutral-beam-injected ionized particles. Because the ions move with a larger gyro-radius than the electrons, the ripple chiefly affects the ions rather than the electrons. For thermal ions, both ripple well transport and ripple banana transport are mainly collisional, referred to as collisional ripple well transport and collisional ripple diffusion, respectively, whereas for fast ions also collisionless transport mechanisms are possible. [48]

For a reactor, the main considerations regarding toroidal magnetic field ripple are losses of particles and associated heat loads. Losses of fast alpha particles can cause highly localized heat loads on the first wall of the tokamak and in-vessel components and thus cause damage to these structures. Losses of neutral-beam-injected fast particles can also lead to localized heat loads as well as to the loss of a significant proportion of the neutral beam energy, especially for beamlines having large angles with the magnetic field.

1.7 JET and ITER on the Path towards Commercialization of Fusion Energy

The numerical modelling presented in subsequent chapters of this thesis has to a significant extent been carried out at the Joint European Torus (JET) [49] at Culham, United Kingdom. The JET facilities, which are operated by the United Kingdom Atomic Energy Authority under the auspices of the European Fusion Development Agreement (EFDA) on behalf of the European fusion research associations and Euratom, house what is by many measures the world's best-performing tokamak. In terms of actual physical size, JET is one of the two largest tokamaks in the world of roughly equal size, the Japanese JT-60U [50] tokamak being the other one. The JET tokamak, casually referred to simply as JET, has a major radius of about 3 m and a plasma volume of about 100 m^3. JET can, in principle, subject to numerous restrictions, operate with a toroidal magnetic field of up to 3.45 T and a plasma current of up to 4.8 MA. Auxiliary plasma heating is available in the form of up to 23 MW of neutral beam injection heating and up to 15 MW of various kinds of radio frequency heating.

Most importantly, JET plays a crucial role in preparing the way for what is foreseen to be the next big step forward in fusion research, the construction and operation of ITER, not least because it features the most ITER-like conditions of all present-day tokamaks in a number of respects. The mission of ITER itself, on the other hand, is arguably even more crucially to unambiguously demonstrate the scientific and technical viability of the tokamak concept in a device with a size, magnetic field strength, physics phenomenology, and technological basis close to that of an

eventual thermonuclear power reactor. Sizewise, the linear dimensions of ITER are to exceed those of JET by more than a factor of two, with the major radius having been set to 6.2 m, from which follows a plasma volume of 840 m^3. ITER is foreseen to operate with a toroidal magnetic field of 5.3 T and a plasma current of 15 MA in the reference ELMy H-mode inductive scenario. The fusion power output is foreseen to be up to 500 MW with a net power gain with respect to the externally injected power of a factor up to $Q = 10$ during up to 400 s long pulses. If ITER meets its objectives of successfully testing all the technologies and resolving all the physics issues necessary for a commercial power plant and thereby demonstrates the viability of fusion power for large scale electricity generation, the final step before full-scale commercialization is envisaged to be the construction of a demonstration power plant tentatively named DEMO.

ITER thus plays a pivotal role on the circuitous path towards commercial fusion energy, and JET on the somewhat less unnavigable path towards ITER. The principal topics of this thesis, the phenomenology and effect of ELMs and the influence of toroidal magnetic field ripple on plasma performance and ELMs are all highly ITER-relevant topics that have been explored at JET in preparation for ITER. In the case of ELMs, the most serious concern is potential damage on the divertor target plates and elsewhere from the large heat loads resulting from type I ELMs, whereas toroidal magnetic field ripple is a cause for concern because recent experiments at JET and the Japanese JT-60U tokamak indicate that the level of ripple foreseen for ITER may have a considerably more detrimental effect on confinement than previously thought [51].

1.8 Scope of the Thesis

This thesis addresses a number of timely problems, all of them of crucial importance on the way towards a commercial fusion reactor: Given the importance of ELMs, the thesis seeks to introduce suitable schemes and models for qualitative study of the ELM phenomenon in predictive transport modelling. It aims to shed new light on the dynamics of ELMs using these models. Understanding the dynamics of ELMs is a key issue when it comes to controlling and mitigating the ELMs in future large tokamaks. The thesis tries, again making use of the aforementioned ELM modelling schemes, to explain various experimental observations, notably the loss of plasma performance and increased ELM frequency observed in experiments with enhanced toroidal magnetic field ripple and in situations with strong external neutral gas puffing. Understanding these results may have implications for the control of ELMs and plasma performance in future tokamaks. Finally, the thesis also tries to establish more generally the potential effects of ripple-induced thermal ion losses on H-mode plasma performance and ELMs. This is a timely and crucial area of

research, given that ITER is foreseen to operate with a level of toroidal magnetic field ripple considerably higher than that at JET.

The present chapter in the thesis has provided a gentle introduction to the physics phenomenology relevant to the topics discussed in subsequent chapters and the results section in particular. Chapter 2 then provides an introduction to the techniques of integrated modelling and contains descriptions of the numerical tools used in the analysis. The main results of the thesis are presented in Chapter 3. Chapter 4 finishes off with a summary and a discussion of the relevance of these results and how they fit into the bigger picture of the European fusion programme with JET preparing the ground for ITER and ITER paving the way for an eventual commercial fusion power plant.

Chapter 2

Numerical Codes and Models

2.1 Integrated Modelling

Predictive transport modelling is a discipline of numerical plasma physics modelling, in which qualitative predictions and explanations for various effects are sought by running transport codes equipped with appropriately chosen models for transport and other relevant phenomena. Traditionally, the plasma core, ETB and SOL have been treated separately in predictive modelling with the justification that the physics governing transport in these regions is different [52]. Indeed, core transport is usually dominated by drift-type plasma turbulence, which is responsible for phenomena such as profile stiffness. In contrast, anomalous transport within the edge ETB is reduced or even completely suppressed by strong shear in plasma rotation. The reduced transport then generates the strong pressure gradient and large edge current characterizing the pedestal, both of which give rise to MHD instabilities thought to generate ELMs. Finally, transport in the SOL is dominated by very fast losses along the field lines and by atomic physics processes, including the interaction between the plasma and neutrals. The disparate time-scales of the phenomena involved adds a formidable complication to the modelling of all three plasma regions in an integrated fashion. Because of this disparity, modelling of the plasma core has conventionally excluded simulation of the ETB. Instead, the values of the relevant plasma parameters at the top of ETB have been used as boundary conditions.

Modelling the core plasma separately from the ETB is, however, not self-consistent because of the strong link between these regions due to effects such as profile stiffness. For this reason, modern core transport codes often feature a representation of the ETB, so that the entire confined plasma inside the separatrix can be modelled in an integrated fashion. This strategy makes it possible at least on a qualitative level to

study a wide variety of effects, in which the interaction between the ETB and the core is important.

In addition to this, there is also a strong link between the ETB and the SOL. Core and edge transport codes usually use static or time-dependent boundary conditions at the separatrix for the parameters such as densities, temperatures and heat fluxes. The problem is that even when time-evolving boundary conditions are available, there is no way to evolve them self-consistently in response to plasma behaviour. Especially during transients such as ELMs the plasma parameters typically used as boundary conditions can change dramatically. Often even a modest variation of the plasma parameters in one region can lead to a dramatic change in plasma performance. Because of the sensitive links between the SOL and the ETB on the one hand and between the ETB and the core on the other hand, integrated modelling of all three plasma regions is often the only way to obtain self-consistent results.

In many cases, integrated modelling also requires the use of tools beyond transport codes. It is customary, for instance, to use MHD stability codes to evaluate stability limits for transport simulations. Another example is the use of orbit-following codes for the purpose of evaluating transport coefficients for transport simulations. In Ref. [53], the author of this thesis reviews current methods and trends in integrated modelling as well as gives a summary of recent developments in the field.

The work presented in this thesis has been carried out using a number of numerical codes. Below follows short descriptions of each of these codes.

2.2 JETTO

Most of the work presented in subsequent sections has been carried out using the 1.5-dimensional (1.5D) core transport code JETTO [54], which has been developed by a team at the JET tokamak over a number of years. Here, the term 1.5D is used to express the fact that a one-dimensional code effectively solves a two-dimensional problem. Given that the magnetic field lines trace surfaces of constant pressure, so-called flux surfaces, the task of solving the transport equations in the poloidal plane reduces to a one-dimensional problem, if the problem is re-expressed using the magnetic flux through these magnetic surfaces as the co-ordinate.

2.2.1 Fundamental Equations

As the term transport code implies, JETTO solves equations for plasma transport. These equations can be derived from first principles, starting from a kinetic description of the plasma, in which the positions and velocities of the individual particles are described statistically by a distribution function $f_s(\vec{x}, \vec{v}, t)$, where the subscript s refers to the particle species [55].

The distribution function $f_s(\vec{x}, \vec{v}, t)$ is a measure of the number particles of a given species per unit volume of the six dimensional spatial-velocity phase space $(\vec{x}, \vec{v}, t)$ as a function of the spatial and velocity co-ordinates. Since the distribution function expresses the number density of particles in phase space, it obeys the conservation equation

$$\frac{\partial f_s}{\partial t} + \frac{\partial f_s}{\partial \vec{x}}\frac{d\vec{x}}{dt} + \frac{\partial f_s}{\partial \vec{v}}\frac{d\vec{v}}{dt} = C(f_s) + S. \tag{2.1}$$

Here, S represents sources and sinks and the term $C(f_s)$ is a collision term derived on the basis of multiple small angle collisions, the exact form of which is derived elsewhere [6].

By making use of the equation of motion for a charged particle of species s in an electric field $\vec{E}$ and magnetic field $\vec{B}$

$$m_s\frac{d\vec{v}}{dt} = e_s(\vec{E} + \vec{v} \times \vec{B}), \tag{2.2}$$

Eq. (2.1) can be turned into the Fokker-Planck equation:

$$\frac{\partial f_s}{\partial t} + \vec{v} \cdot \frac{\partial f_s}{\partial \vec{x}} + \frac{e_s}{m_s}(\vec{E} + \vec{v} \times \vec{B}) \cdot \frac{\partial f_s}{\partial \vec{v}} = C(f_s) + S. \tag{2.3}$$

Here, m_s is the mass and e_s the charge of a particle of species s.

Taking velocity moments of the Fokker-Planck equation, i.e. multiplying it by a given power of $|\vec{v}|$ and integrating it over velocity space, gives a series of so-called moment equations, from which conservation laws describing plasma transport can be derived. In particular, taking the zeroth moment of the Fokker-Planck equation, i.e. integrating it over velocity space, gives after some algebra

$$\frac{\partial n_s}{\partial t} + \nabla \cdot (n_s\vec{u}_s) = 0, \tag{2.4}$$

a result known as the continuity equation. Here, $n_s = \int f_s(\vec{x}, \vec{v}, t)d\vec{v}$ is the particle density of species s given the distribution function f_s for that species and $\vec{u}_s$ is the fluid velocity. Similarly, taking the $|\vec{v}|^2$ moment of the Fokker-Planck equation, i.e. multiplying it by $|\vec{v}|^2$ and integrating the resulting equation over velocity space, yields after some algebraic manipulation

$$\frac{3}{2}\frac{\partial p_s}{\partial t} + \nabla \cdot \vec{\mathcal{Q}}_s = \mathcal{Q}_s + \vec{u}_s \cdot (\vec{F}_s + e_s n_s \vec{E}). \tag{2.5}$$

Here, $p_s = n_s T_s = (1/3)\mathrm{tr}(\int m_s \vec{v}\vec{v} f_s(\vec{x},\vec{v},t) d^3\vec{v})$ is the plasma pressure of species s, $\vec{\mathcal{Q}}_s = \int (m_s/2)|\vec{v}|^2 \vec{v} f_s(\vec{x},\vec{v},t) d^3\vec{v}$ is the energy flux associated with species s, $\mathcal{Q}_s = \int (m_s/2)|\vec{v}-\vec{u}_s|^2 C(f_s) d^3\vec{v}$ is the collisional energy exchange associated with species s and $\vec{F}_s = \int m_s \vec{v} C(f_s) d^3\vec{v}$ is the collisional momentum exchange or friction force associated with species s.

By integrating the continuity equation, Eq. (2.4), over a region interior to a flux surface and using the divergence theorem $\int \nabla \cdot \mathcal{F} dV = \oint \mathcal{F} \cdot d\vec{A}$ for an arbitrary continuously differentiable function $\mathcal{F}$, the equation can after some algebraic manipulation be cast into the following particle conservation law, which can be written for each main ion species $i = 1, ..., n_H$:

$$\left(\frac{\partial V}{\partial \rho}\right)^{-1} \frac{\partial}{\partial t}\left(\frac{\partial V}{\partial \rho} n_i\right) + \left(\frac{\partial V}{\partial \rho}\right)^{-1} \frac{\partial}{\partial \rho}\left(\frac{\partial V}{\partial \rho}\Gamma_i\right) = \langle S_{ni}\rangle. \tag{2.6}$$

Analogous equations can be derived for each impurity ion species $I = 1, ..., n_{imp}$ in the plasma:

$$\left(\frac{\partial V}{\partial \rho}\right)^{-1} \frac{\partial}{\partial t}\left(\frac{\partial V}{\partial \rho} n_{imp}\right) + \left(\frac{\partial V}{\partial \rho}\right)^{-1} \frac{\partial}{\partial \rho}\left(\frac{\partial V}{\partial \rho}\Gamma_{imp}\right) = 0. \tag{2.7}$$

In a similar way, the $|\vec{v}|^2$ moment equation, Eq. (2.5), can be turned into energy conservation laws for the electron and ion species:

$$\begin{aligned} &\frac{3}{2}\left(\frac{\partial V}{\partial \rho}\right)^{-5/3} \frac{\partial}{\partial t}\left[\left(\frac{\partial V}{\partial \rho}\right)^{5/3} p_e\right] + \left(\frac{\partial V}{\partial \rho}\right)^{-1} \frac{\partial}{\partial \rho}\left[\frac{\partial V}{\partial \rho}\left(\langle \vec{q_e} \cdot \nabla\rho\rangle + \frac{5}{2} T_e \Gamma_e\right)\right] \\ &= -\sum_{i=1}^{n_H} \langle \mathcal{Q}_{i\Delta}\rangle - \sum_{i=1}^{n_H} \langle \mathcal{Q}_{i\Gamma}\rangle + \langle \vec{j}\cdot\vec{E}\rangle + \langle S_{Ee}\rangle \end{aligned} \tag{2.8}$$

$$\begin{aligned} &\frac{3}{2}\left(\frac{\partial V}{\partial \rho}\right)^{-5/3} \frac{\partial}{\partial t}\left[\left(\frac{\partial V}{\partial \rho}\right)^{5/3} \sum_{i=1}^{n_H} p_i\right] + \left(\frac{\partial V}{\partial \rho}\right)^{-1} \frac{\partial}{\partial \rho}\left[\frac{\partial V}{\partial \rho}\sum_{i=1}^{n_H}\left(\langle \vec{q_i} \cdot \nabla\rho\rangle + \frac{5}{2} T_i \Gamma_i\right)\right] \\ &= \sum_{i=1}^{n_H} \langle \mathcal{Q}_{i\Delta}\rangle + \sum_{i=1}^{n_H} \langle \mathcal{Q}_{i\Gamma}\rangle + \langle S_{Ei}\rangle \end{aligned} \tag{2.9}$$

In the equations above, ρ is a radial co-ordinate with the dimension of length proportional to the square root of the normalized toroidal magnetic flux through the surface of constant magnetic flux defined by ρ, $V = V(\rho)$ is the plasma volume inside the magnetic surface ρ and Γ_s is the particle flux associated with species s. The terms on the right-hand sides of the equations are source terms. Specifically, $\langle S_{ni}\rangle$ is the external particle source, $\langle \mathcal{Q}_{i\Delta}\rangle$ is the averaged energy exchange term between the electrons and ions of species i, $\langle \mathcal{Q}_{i\Gamma}\rangle$ is an averaged convective source term, $\langle \vec{j}\cdot\vec{E}\rangle$, where $\vec{j}$ is the plasma current, is the Ohmic heating source and $\langle S_{Ee}\rangle$ and $\langle S_{Ei}\rangle$ are external heat sources or sinks due to background neutrals, radiation, auxiliary power input, etc.

It should also be noted that in Eq. (2.8), the average electron energy flux $\langle \vec{\mathcal{Q}}_e \cdot \nabla\rho \rangle$ has been split up into a conductive part due to thermal transport and a convective part due to particle convection: $\langle \vec{\mathcal{Q}}_e \cdot \nabla\rho \rangle = \langle \vec{q}_e \cdot \nabla\rho \rangle + (5/2)T_e\Gamma_e$. In a similar way, the average ion energy flux of each ion species in Eq. (2.9) has been split up into conductive and convective parts: $\langle \vec{\mathcal{Q}}_i \cdot \nabla\rho \rangle = \langle \vec{q}_i \cdot \nabla\rho \rangle + (5/2)T_i\Gamma_i$.

The conservation laws defined by Eqs. (2.6) – (2.9), derived from first principles, are also known as transport equations. JETTO solves these equations at each time step. In addition to the transport equations, JETTO solves a version of Faraday's equation

$$\nabla \times \vec{E} = -\frac{\partial \vec{B}}{\partial t}, \tag{2.10}$$

a fundamental equation relating the electric field $\vec{E}$ and magnetic field $\vec{B}$, and an equation for the magnetic equilibrium known as the Grad-Shafranov equation [6]:

$$R\frac{\partial}{\partial R}\frac{1}{R}\frac{\partial \Psi}{\partial R} + \frac{\partial^2 \Psi}{\partial z^2} = -\mu_0 R^2 \frac{dp}{d\Psi} - \mu_0^2 f \frac{df}{d\Psi} \tag{2.11}$$

The Grad-Shafranov equation is a first-principles equation from which the distribution of the magnetic flux surfaces can be solved. The equation can be derived starting from the magnetic equilibrium equation

$$j \times B = \nabla p, \tag{2.12}$$

where j is the current density, B the magnetic field and p the plasma pressure, and by expressing the poloidal magnetic field B_θ and the poloidal current density j_θ in terms of a poloidal flux function Ψ and a current flux function $f = RB_\phi/\mu_0$, where R is the major radius and B_ϕ the toroidal magnetic field: $\vec{B_\theta} = \nabla\Psi \times \vec{u_\phi}/R$ and $\vec{j_\theta} = \nabla f \times \vec{u_\phi}/R$, where $\vec{u_\phi}$ is a unit vector in the toroidal direction. The magnetic equilibrium equation expresses the basic condition that the magnetic force balances the force due to the plasma pressure at all locations in the plasma.

A technical detail worth mentioning is that in a JETTO run the Grad-Shafranov equation is actually solved by a separate code known as ESCO, an MHD equilibrium solver which has been linked to JETTO. An alternative way to deal with the problem, available in JETTO, is to read in the equilibrium solution from data provided by the equilibrium reconstruction code EFIT [56], which is widely used at many tokamaks. The equilibrium is always provided at the beginning of a simulation and can be recalculated later as many times as needed.

2.2.2 Transport Model

The fundamental equations presented above, which are solved by JETTO, describe the evolution of the confined plasma in a rigorous, completely self-consistent way

based on first principles. Customarily, transport codes such as JETTO are used to predict the temporal evolution of the density and temperature profiles. Given that the density n_s and temperature T_s of a given particle species s are related to each other through the relation $p_s = n_s T_s$, where p_s is the pressure attributable to that species, solving Eqs. (2.6) – (2.9) for the density and temperature profiles requires knowledge of the heat fluxes q_s and particle fluxes Γ_s, in addition to knowledge of the source terms in these equations. To put it slightly differently, the solution of the transport equations depends on the plasma transport properties, which determine the heat and particle fluxes in these equations. Calculating the fluxes, on the other hand, requires some sort of model, given that a kinetic treatment is not practicable. This is where the concept of a transport model comes in. The heat fluxes can be expressed as

$$q_e = -\chi_e n_e \nabla T_e \tag{2.13}$$

and

$$q_i = -\chi_I n_i \nabla T_I. \tag{2.14}$$

In the above expressions, χ_e is the electron thermal conductivity and χ_I is the ion thermal conductivity. It should be noted that it is here assumed that the ion thermal conductivity χ_I is not species-specific but a common quantity for all ion species and that, analogously, T_I is a common temperature of all the ion species.

The particle fluxes can be expressed in a similar way. The particle flux of ions of species i can be expressed as

$$\Gamma_i = -D_i \nabla n_i + \Gamma_{inw,i} + \Gamma_{ware,i}, \tag{2.15}$$

and, because of ambipolarity, the electron particle flux then takes the form:

$$\Gamma_e = -\sum_{i=1}^{n_H} Z_i \left(D_i \nabla n_i + \Gamma_{inw,i} + \Gamma_{ware,i} \right). \tag{2.16}$$

Here, D_i is the particle diffusivity of ion species i and Z_i is the atomic number of ion species i. The term $\Gamma_{inw,i}$ is an inward advection term [22] and the term $\Gamma_{ware,i}$ represents the neo-classical Ware pinch [57].

The particle diffusivities D_i for the various ion species, the ion thermal conductivity χ_I, the electron thermal conductivity χ_e, which are generally both spatial and temporal functions, are called transport coefficients, because they describe the transport properties of the plasma. It is customary to try to express the transport coefficients in terms of a transport model. JETTO includes a number of models, both theoretical and semi-empirical ones, for predicting these so-called transport coefficients.

Generally, the transport coefficients in a transport model can be made up of several contributions arising from different sources of transport. To begin with, the

transport coefficients may include contributions due to neo-classical transport. As discussed in Chapter 1, the neo-classical contribution is theoretically completely rigid, but is typically more than an order of magnitude smaller than the actual level of transport measured in tokamaks. Accordingly, the main contributions to the transport coefficients have to represent anomalous transport, the theoretically not fully understood transport due to micro-turbulence arising e.g. from the application of external heating. Various theoretical models for the properties of turbulence have been proposed [58], but generally these are not fully complete, and therefore do not necessarily give accurate predictions for the transport coefficients in all situations. For this reason, semi-empirical models have been used in many studies. In these models, theory-based expressions for the general form of the transport coefficients have been calibrated against experimental data.

All the JETTO simulations discussed in this work use a semi-empirical so-called Bohm/gyro-Bohm model for anomalous transport, which is applied on top of contributions due to neo-classical transport. This class of models was originally developed at the JET tokamak for L-mode plasmas and calibrated against a large number of discharges, and has since then been refined for use with H-mode plasmas [59, 60]. The Bohm/gyro-Bohm model includes contributions from a Bohm term large especially at the edge but of significant magnitude throughout the plasma and a gyro-Bohm term, which contributes only in the deep core. Gyro-Bohm-type transport follows from short-wavelength turbulence, whereas Bohm-type transport is due to turbulence scaling with the machine size [61]. The neo-classical contributions to the transport coefficients are calculated by a module known as NCLASS [62], which has been linked to JETTO.

Specifically, the Bohm/gyro-Bohm transport model combined with neo-classical contributions that has been used in the work presented in subsequent chapters can be written as follows:

$$\chi_e = \chi_{Bohm,\ e} + \chi_{gyro-Bohm} + \chi_{neo-classical,\ e} \tag{2.17}$$

$$\chi_I = \chi_{Bohm,\ I} + \chi_{gyro-Bohm} + \chi_{neo-classical,\ I} \tag{2.18}$$

$$\chi_{Bohm,\ e} = \alpha_{Bohm} \frac{q^2}{eB_\phi n_e} \left| \frac{dp_e}{d\rho} \right| \frac{T_e(\rho_{ToB}) - T_e(1)}{T_e(\rho_{ToB})} \tag{2.19}$$

$$\chi_{Bohm,\ I} = 2\chi_{Bohm,\ e} \tag{2.20}$$

$$\chi_{gyro-Bohm} = \alpha_{gyro-Bohm} \frac{\sqrt{T_e}}{B_\phi^2} |\nabla T_e| \tag{2.21}$$

Here, $\chi_{neo-classical,\ s}$ is the neo-classical transport of species s given by the module NCLASS and ρ_{ToB} is the location of the top of the pedestal in terms of the ρ coordinate.

The transport model defined by Eqs. (2.17) – (2.21) does a relatively good job when it comes to predicting the transport coefficients in the core plasma inside the

ETB in an H-mode discharge. The model, however, does not take into account the formation of an ETB – understandably – because the almost complete suppression of anomalous transport in this narrow layer just inside the separatrix is very hard to predict theoretically. Therefore, JETTO includes a separate model for the ETB. The ETB is simply represented by a reduction of all transport coefficients to the ion neo-classical level in the region just inside the separatrix. In the work reported in this thesis, the width of the ETB is a free parameter, which has generally been set to match experimental observations. Various models for the ETB width have been proposed, including a barrier width scaling proportionally with the square root of the poloidal β [63] or with the local thermal gyro-radius or fast particle gyro-radius, but especially the latter ones are generally not considered very reliable. Even though JETTO includes implementations of such models, only the *ad hoc* model in which the ETB is a free parameter has been used in the work presented in this thesis.

The semi-empirical Bohm/gyro-Bohm transport model combined with the *ad hoc* ETB model described above gives a reasonably realistic description of the plasma transport properties in the absence of spurious events such as ELMs. A broadly held view is that transport within and in the vicinity of the ETB increases dramatically during ELMs. It is thought that the MHD instabilities believed to drive the ELMs give rise to a massive increase in the level of transport in this region and that it is this increase in transport that causes the sudden expulsion of energy and particles into the SOL. To date, this intermittent increase in transport believed to occur during the ELMs is poorly understood, and, consequently, no self-consistent model with a good predictive capability exists for it.

One of the problems tackled in this thesis is, under the assumption that the ELM is a transport phenomenon, to develop ELM models useful in predictive transport modelling aimed at qualitatively studying various phenomena. The models proposed in this thesis are described in detail in the first few sections of Chapter 3. The thesis then continues with the application of these models to a range of physics problems.

It should be noted that ELMs are not the only type of intermittency not taken into account by the Bohm/gyro-Bohm and ETB models. Other types of spurious events are common in fusion plasmas, notably sawtooth oscillations, which are a type of intermittent burst of particles and energy in the deep core, believed like ELMs to be transport events driven by MHD instabilities. Given that this thesis deals solely with qualitative phenomena occurring in the edge plasma, models for transient events other than ELMs have been omitted, for simplicity. Qualitatively, this should not influence the results and the conclusions drawn from them.

2.2.3 Auxiliary Modules

Finally, it should be stressed that JETTO is more than a transport solver. Several external modules have been coupled to JETTO for dealing with physics affecting the outcome of the transport calculation at the core of the code. For the power deposition and beam-driven current distribution due to neutral beam injection (NBI) heating, a package called PENCIL [64] is used. PENCIL calculates the dynamics of the fast ion distribution from the Fokker-Planck equation. Alternatively, the power deposition profiles can be read in as data produced by external means. JETTO also includes numerical codes for other plasma heating methods such as ion cyclotron resonance frequency heating (ICRH) [10], electron cyclotron resonance frequency heating (ECRH) [65–67] and lower hybrid heating and current drive (LHCD) [10]. For transport of neutral particles, there is a package called FRANTIC [68] linked to JETTO. FRANTIC is a Monte Carlo code [69, 70], which means that it uses algorithms relying on repeated random sampling to compute their results.

2.3 COCONUT

Apart from JETTO, a considerably more complex transport code known as COCONUT [71] has been used in certain well-defined parts of the work described in subsequent sections. COCONUT, which is also provided by JET is, in fact, a coupling of the 1.5D core transport code JETTO and the 2D edge transport code EDGE2D [72]. Such a coupling of two codes working in different plasma regions is necessary for self-consistent modelling of the entire plasma, as described in Sec. 2.1.

In the COCONUT coupling, JETTO works as described in the previous subsection. The other code, EDGE2D works on a two-dimensional grid at the edge. Figure 2.1 provides an illustration of the EDGE2D simulation domain and typical simulation grid. The code requires a mesh consisting of quadrilaterals with two sides parallel to the flux surfaces. Typically, the boundary between the simulation domains of JETTO and EDGE2D in a COCONUT run is at the separatrix. EDGE2D passes the heat and particle fluxes across the separatrix as boundary conditions for JETTO and, similarly, JETTO passes the same quantities as boundary conditions for EDGE2D. In this way, both JETTO and EDGE2D are provided with self-consistent boundary conditions.

Given the two-dimensional nature of SOL physics, EDGE2D is an even more complex tool than JETTO. In brief, EDGE2D solves a set of single-fluid equations similar to the set of equations solved by JETTO. Here, the term single fluid means that from an MHD point of view, the plasma is treated as a single quasi-neutral fluid of electrons and ions. Specifically, EDGE2D solves continuity equations for the conservation of

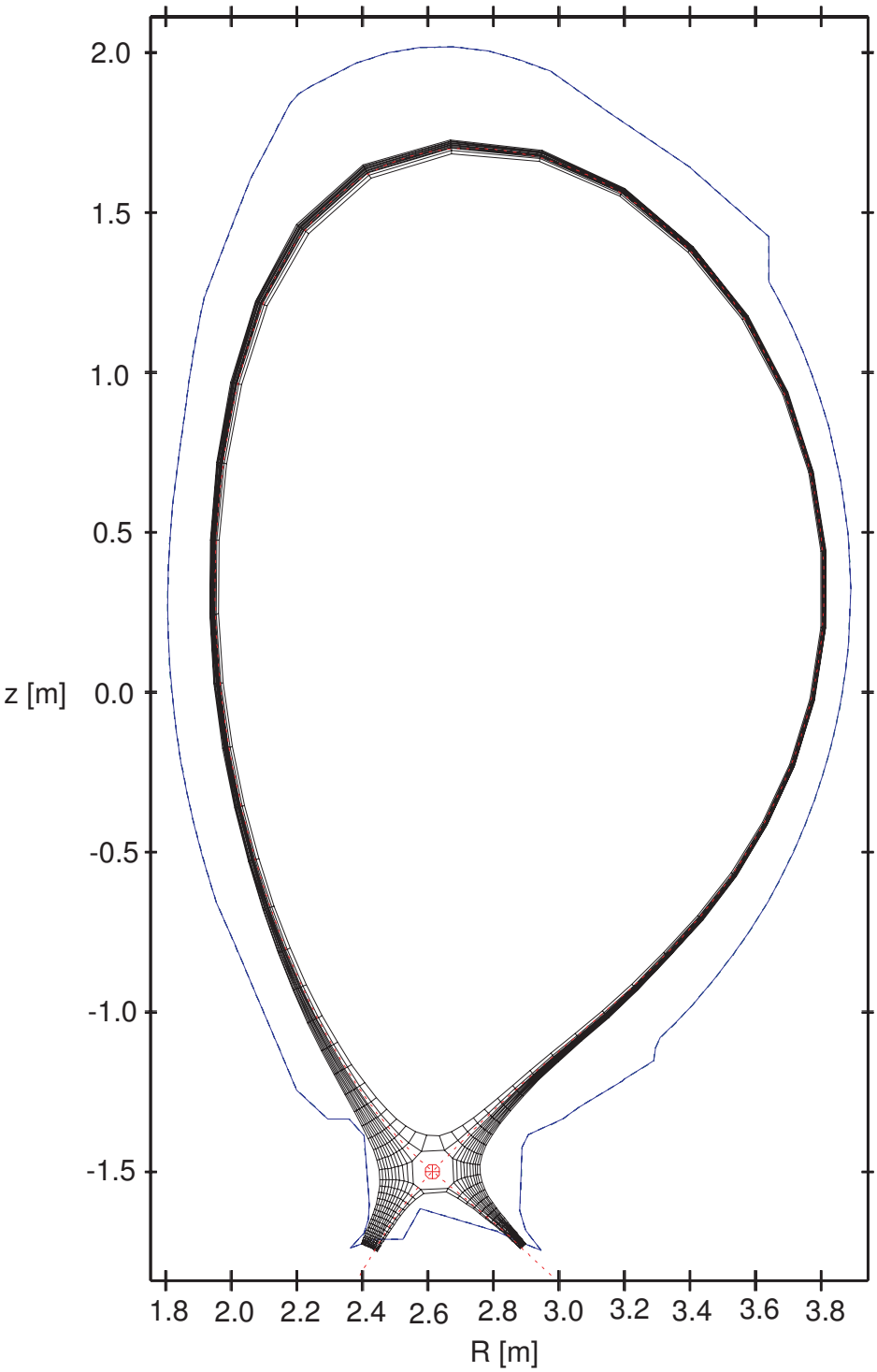

Figure 2.1: *A typical EDGE2D simulation grid consisting of quadrilaterals with two sides parallel to the flux surfaces. The solid blue line outside the grid itself denotes the vessel wall. The dotted red line indicates the magnetic separatrix. The grid is for a JET low-triangularity equilibrium.*

particles, energy conservation equations and momentum conservation equations for electrons, one hydrogenic ion species and up to two impurity species. Given that the transport equations in EDGE2D are essentially variants of the conservation laws derived in Sec. 2.2.1 which JETTO solves, the exact expressions will not be listed here, but are given in Ref. [72]. In addition to that, the same equations can be found in the more detailed Ref. [73], which contains extensively detailed descriptions about issues related to two-dimensional edge fluid codes generally applicable to EDGE2D.

It should be emphasized that the transport equations solved by EDGE2D are fundamental conservation laws derived from first principles. As in JETTO, the heat and particle fluxes appearing in the fundamental equations are calculated using transport coefficients that determine these fluxes. Again, various transport models can be used for evaluating the transport coefficients. A difference with respect to JETTO is that EDGE2D solves the transport equations in two dimensions and therefore has to deal with transport both perpendicular and parallel to the magnetic field lines. Perpendicular transport is assumed to be anomalous transport due to magnetic turbulence. In the work presented in this thesis, the perpendicular transport coefficients have simply been given *ad hoc* values, because very little is known about what values and what kind of spatial behaviour these coefficients actually might have in a real plasma. Often, the inter-ELM ion neo-classical level of perpendicular transport at the top of the pedestal in JETTO has simply been used radially and poloidally uniformly for the SOL in EDGE2D as well.

Parallel transport, which is better understood, is treated classically in EDGE2D. The classical parallel transport coefficients are calculated using a discretization technique known as the 21-moment approximation [74]. On top of this, the parallel transport coefficients can be scaled by adjusting transmission factors known as the ion heat flux limiting factor $\alpha_{flux,i}$ and the electron heat flux limiting factor $\alpha_{flux,e}$ and defined as [73]

$$\chi_{\parallel,s} = \frac{\chi_{\parallel 0,s}}{1 + \left| \frac{n_s \chi_{\parallel 0,s} \nabla T_s}{\alpha_{flux,s} n_s c_s T_s} \right|}. \tag{2.22}$$

Here, the subscript s stands for either ions i or electrons e, $\chi_{\parallel 0,s}$ is the thermal conductivity in the direction parallel to the field lines given by the 21-moment approximation, $\chi_{\parallel,s}$ is the modified thermal conductivity in the direction parallel to the field lines and c_s is the sound speed. The heat flux limiting factors, which as the name implies limit the heat fluxes appearing in the transport equations, are a way of describing a transition from diffusive to convective transport. There is also available a second set of transmission coefficients known as the ion and electron sheath heat transmission coefficients, which like the heat flux limiting factors can be used as kinetic corrections to the fluid treatment.

For dealing with the interactions of hot neutrals with the background plasma, EDGE2D in itself has traditionally been linked to a kinetic neutral particle Monte Carlo code known as NIMBUS [75] and is, therefore, often referred to as EDGE2D/

NIMBUS. Recently, NIMBUS has been replaced with a more advanced code known as EIRENE [76], and, consequently, it is customary to talk about EDGE2D/EIRENE when referring to this combination.

2.4 ASCOT

For estimating the effect of ripple losses of thermal ions on transport, a Monte Carlo orbit-following code called ASCOT [77] has been used. ASCOT is provided by Helsinki University of Technology and is available at JET.

In ASCOT simulations, an ensemble of test particles represents a population of physical particles. By using a special particle weighing scheme, each test particle represents a large number of physical particles. The test particles are simulated on top of a stationary background plasma with a locally Maxwellian velocity distribution.

The motion of charged particles in a magnetic field follows from the (non-relativistic) Lorentz force given by Eq. (2.2) that the individual particles experience. As noted earlier, it can easily be shown that this equation leads to gyro-motion for a charged particle in a magnetic field. Furthermore, it can be shown, again starting from Eq. (2.2), that the guiding centre of the particle orbit experiences various drifts known as $\vec{E}_r \times \vec{B}$, polarization, gradient and curvature drifts under the influence of electric and magnetic fields [6]. ASCOT is a guiding centre following code, which means that it averages out the gyro-motion and follows only the guiding centres of the gyrating particles.

Collisions, or more generally speaking interactions, between the test particles and background plasma are evaluated between the orbit integration time steps. The interactions are modelled by a Monte Carlo collision operator based on a binomial probability distribution. The effect of a toroidal electric field, however, is deterministic. ASCOT takes into account various physics processes such as neo-classical effects including collisional transport, finite orbit width effects and trapped particle effects, losses such as orbit losses and charge exchange losses, and beam thermal diffusion.

ASCOT has a three-dimensional model for magnetic ripple [78], enabling realistic estimates for ripple losses to be obtained including the localization of the losses as a function of the ripple amplitude, plasma parameters and magnetic configuration.

2.5 MHD Stability Codes

The above described codes JETTO, COCONUT and ASCOT all in their own ways deal with transport and in particular with constructing and applying models for thermal and particle diffusivity. Because separate models for intermittency such as ELMs are to be applied when the plasma is thought to become unstable, the MHD stability of the plasma also has to be taken into account. The transport analysis presented in subsequent chapters often makes use of MHD stability results. The MHD stability calculations have been carried out using two codes called HELENA [79] and MISHKA-1 [80].

2.5.1 HELENA

HELENA is an MHD equilibrium solver, i.e. it solves the Grad-Shafranov equation for the distribution of the magnetic flux surfaces. HELENA has been used for solving the magnetic equilibrium with a higher resolution than what is available from JETTO's internal equilibrium solver ESCO in order to provide MISHKA with an adequately refined equilibrium solution. HELENA also solves for stability against infinite-n ballooning modes.

2.5.2 MISHKA

MISHKA is a linear MHD stability code, available in many versions. In the work presented in subsequent chapters, an ideal linear version called MISHKA-1 has been used almost exclusively. MISHKA-1 solves a set of ideal linear MHD equations and can evaluate stability against any mode number, providing growth rates and eigenfunctions as output. Given that MISHKA plays an auxiliary role in the work discussed in subsequent chapters, the rather lengthy details of the equations solved by the code are omitted here. A full description of MISHKA can be found in Ref. [80].

Chapter 3

Predictive Transport Modelling of Edge Transport Processes in ELMy H-Mode Tokamak Plasmas

The main results of the thesis are presented in this chapter. As described in the previous chapter, the Bohm/gyro-Bohm model in combination with the *ad hoc* ETB model in JETTO is not capable of describing plasma transport during ELMs and other transients events. Consequently, much of the beginning of the present chapter describes ELM models and ELM modelling schemes suitable for predictive transport modelling, which have been developed as part of the thesis work. Subsequent sections then describe results obtained using these models and schemes. Most of the work is core and ETB modelling with JETTO, but there is also a section dealing with integrated modelling using COCONUT. Most of the simulations described in the present chapter have been performed using JET plasmas.

3.1 Modelling with *ad hoc* Models for Type I, Type II and Type III ELMs

Understanding the ELM phenomenon and developing a model for it with predictive capability have been key goals in magnetic fusion research ever since the important role of ELMs in determining plasma confinement and heat loads on plasma-facing components was first understood. Unfortunately, given that the ELM is an exceedingly complex, non-linear phenomenon, these goals are still to a significant extent to be achieved. The physics of ELMs is not fully understood and no universal ELM model exists for numerical modelling purposes. Nevertheless, however intricate it

may be to describe the ELM phenomenon accurately in terms of getting the physics right, simplified and phenomenological models have turned out to be highly useful and versatile in predictive transport modelling. In particular, such models are usually capable of correctly reproducing and predicting qualitative trends such as changes in the ELM frequency and the level of confinement. Even *ad hoc* models, which lack much of the physics of the ELM phenomenon and only try to reproduce its effects, have been used successfully in various studies yielding a plethora of qualitative physics results. Publications 1 and 2 describe a few such results.

3.1.1 MHD Stability Interpretation

As described in Publications 1 and 2, a suite of phenomenological *ad hoc* ELM models suitable for qualitative modelling has been implemented into JETTO and used in predictive transport modelling. These models rely on the common assumptions that the large particle and heat flux during an ELM results from a transport perturbation in the edge plasma and that this edge transport perturbation is driven by MHD instabilities. The MHD stability interpretation on which the models are based is discussed below. Before this discussion, a few concepts need to be clarified, which can most conveniently be done by considering some results obtained in ideal linear MHD stability analysis of JET plasmas.

Figure 3.1, which has been obtained by running MISHKA-1 for a couple of high-triangularity JET equilibria, illustrates what MHD stability diagrams typically may look like and will be used as an aid in the description of ELM models. Here, high-triangularity refers to the shape of the toroidal plasma cross section. Shown in the diagrams are the toroidal mode numbers of the most unstable peeling and ballooning modes as well as infinite-n ballooning instabilities (marked with crosses) in a number of locations in an operational space with the normalized pressure gradient α on the horizontal axis and magnetic shear s on the vertical axis. The operational point (marked with a dot) is also shown. Here, α is defined as $\alpha = -(2\mu_0 r^2/B_\theta)(dp/d\psi)$, where B_θ is the poloidal magnetic field, p is the pressure and ψ is the poloidal flux. The diagram in frame (a) represents a situation with a modest density, whereas frame (b) is for a high-density situation often achieved with high levels of external neutral gas puffing. The qualitative differences between the two diagrams should be noted. In frame (a), the operational point is located in what is referred to as the second ballooning stable regime, a stable regime at intermediate levels of magnetic shear, where stability is limited by medium-n ballooning modes. In frame (b), the operational point appears to be deeply unstable against infinite-n ballooning modes. Stability is effectively limited by what is referred to as the first stability limit, i.e. the left boundary of the infinite-n ballooning unstable region in the diagrams. The stable region left of the infinite-n ballooning unstable region is referred to as the first ballooning stability region.

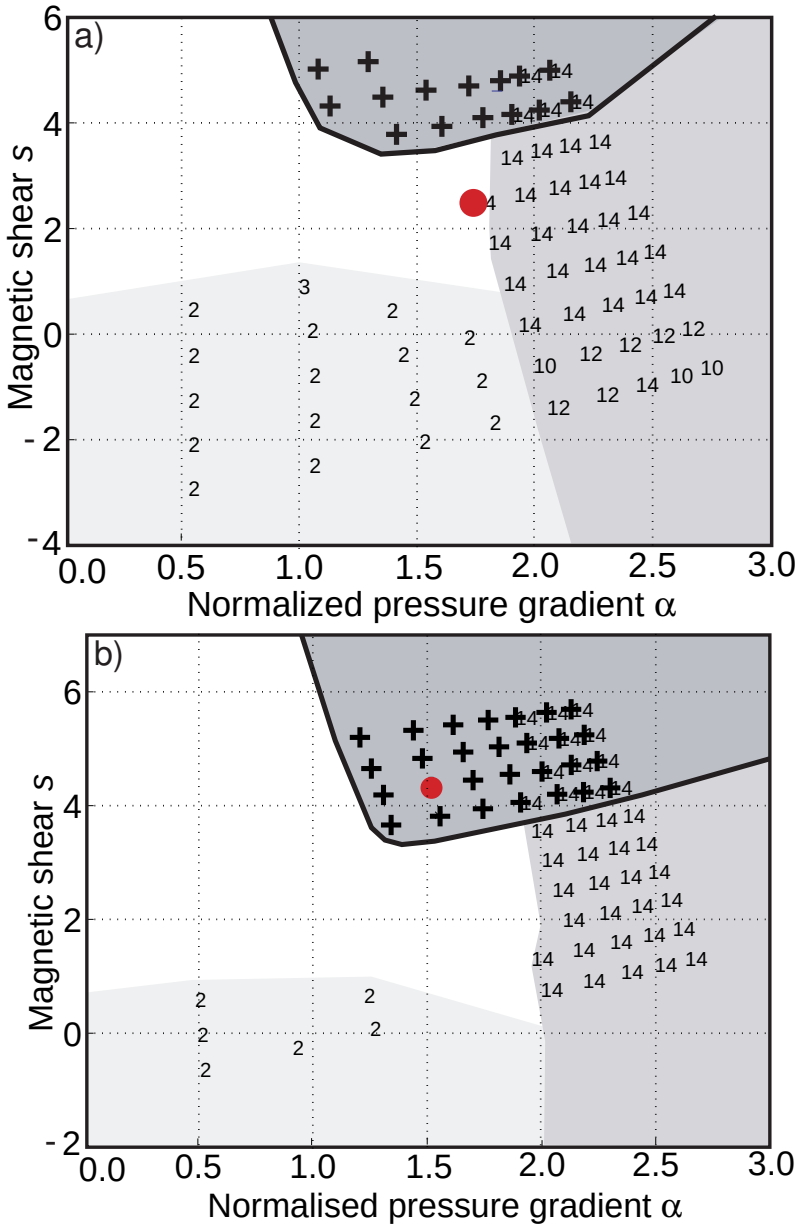

Figure 3.1: *MHD stability diagrams obtained by running MISHKA-1 for JET plasmas: (a) a low-density high-triangularity plasma and (b) a high-density high-triangularity plasma. The diagrams correspond to radial locations near the magnetic surface with the maximum pressure gradient. The numbers on the plot indicate the toroidal mode numbers of the most unstable kink, peeling or ballooning mode in each location. The solid curve marks the infinite-n ballooning stability boundary, inside (above and to the left of) which infinite-n ballooning unstable points (marked with crosses) are found. The operational point is marked with a dot. The approximate areas in the parameter space with infinite-n ballooning, finite-n ballooning and kink/peeling modes have been marked with different shades of grey.*

In Publications 1 and 2, it is argued that a type I ELM occurs when the finite-n ballooning stability limit to the right of the second stable region in the diagrams in Fig. 3.1 is violated. In other words, the situation in frame (a), in which the operational point is located in the second ballooning stability region, and the finite-n ballooning stability limit defines stability and occasionally gets violated, is assumed to represent a type I ELMy H-mode. Similarly, a type III ELM is proposed to occur for higher magnetic shear, when the first ballooning stability limit is violated, with the caveat that stability has to be controlled by the first ballooning stability limit in a region whose radial extent is a sizable fraction of the pedestal width. Thus, the situation in frame (b) in Fig. 3.1, where the plasma is infinite-n ballooning unstable, is interpreted to correspond to a type III ELMy H-mode, provided that the picture is the same for a range of flux surfaces covering most of the pedestal. Violations of the first ballooning stability limit at the outermost flux surfaces only, in a region significantly narrower than the pedestal width, are interpreted to result in type II ELMs at the edge. In accordance with these assumptions, a pure type II ELMy H-mode is proposed to correspond to the following situation: the inner part of the ETB is second ballooning stable and the pressure gradient in this region never builds up to the critical level defined by the finite-n ballooning stability limit, but the outermost edge of the ETB is unstable against infinite-n ballooning modes, with marginal stability in this region being defined by the first ballooning stability limit. Analogously, a mixed mode of operation, referred to as type I-II ELMy H-mode [41, 42], is proposed to correspond to the following situation: the inner part of the ETB is second ballooning stable, but features occasional violations of the finite-n ballooning stability limit, which result in type I ELMs, and the outermost edge of the ETB is unstable against infinite-n ballooning modes causing type II ELMs, with marginal stability in this region again being defined by the first ballooning stability limit. As will become evident later, it is possible to reproduce a number of experimental characteristics correctly with these definitions including the high ELM frequencies in type II and type III ELMy H-modes in comparison to type I ELMy H-mode and the reduced confinement in type III ELMy H-mode, but not in type II ELMy H-mode, with respect to type I ELMy H-mode.

3.1.2 *Ad hoc* ELM Modelling Schemes

In simulations with the phenomenological *ad hoc* ELM models discussed in Publications 1 and 2, the ETB is represented by a reduction of all transport coefficients to a uniform ion neo-classical level. An ELM is triggered when the pressure gradient (typically) anywhere within the pedestal exceeds a pre-defined radially constant critical pressure gradient. During the ELMs, all transport coefficients are increased uniformly within the pedestal to pre-defined levels. The ELM duration and ELM amplitude in terms of the enhanced level of ion thermal conductivity, electron thermal conductivity and particle diffusivity are typically adjusted so that the energy loss per ELM corresponds to experimental observations. In the case of a mixed type

I-II ELMy H-mode, separate stability limits for the outermost and the inner region of the ETB are used. Transport is enhanced only in the region where stability is violated. The transport enhancement factor is kept much smaller in the outer region than in the inner region, in order to account for the fact that type II ELMs are far smaller events than type I ELMs.

Despite their crudeness, the simple models described above are capable of qualitatively reproducing much of the experimental dynamics of the various ELMy H-mode regimes at a level that makes them useful in predictive transport modelling. To begin with, schemes such as these fulfil the basic requirement that they can reproduce an ELM frequency that increases with increasing external heating power. This basic type I ELMy H-mode-like property follows from the fact that the higher the level of absorbed power in the pedestal, the more rapidly the pedestal builds up after an ELM crash, so it is not surprisingly a feature that can be reproduced with very simplistic schemes. The models also tend to be able to reproduce changes in confinement correctly in a qualitative sense when used in predictive transport simulations, as will be seen further on. Publications 1 and 2, among other things, describe some results obtained with the suite of *ad hoc* models. The scheme for modelling type I ELMy H-mode has also been used in Publication 5.

Figure 3.2 illustrates how the *ad hoc* ELM model for type I ELMy H-mode influences the time evolution of the transport coefficients and how the ELM frequency given by the model behaves in response to a change in the external heating power. The figure shows the ion thermal conductivity at the magnetic surface $\rho = 0.97$, a radial location in the middle of the ETB, in two predictive JETTO simulations with different levels of external heating power. The periodic spikes in the level of ion thermal conductivity are type I ELMs triggered by the *ad hoc* ELM model. In the simulation used in frame (a), 16 MW of neutral beam power is injected into the plasma, whereas a level of 8 MW is used in the simulation used in frame (b). The ELM frequency in the former simulation is higher by a factor of almost 1.7.

Figure 3.3 illustrates how the suite of *ad hoc* models qualitatively reproduces the dynamics of mixed type I-II ELMy H-mode, as described in Publication 2. The figure shows time traces of the ion thermal conductivity at the flux surfaces $\rho = 0.995$ and $\rho = 0.965$, which are located on different sides of the boundary between the two pedestal regions associated with type II and type I ELMs, respectively. In accordance with results from MHD stability analysis, different critical pressure gradients and different enhancement factors have been used in the two regions. The time trace for the location close to the separatrix shows tiny, frequent type II ELMs interrupted by occasional large type I ELMs. The behaviour reproduced by the model characteristically resembles the experimentally observed behaviour in mixed type I-II ELMy H-mode regimes.

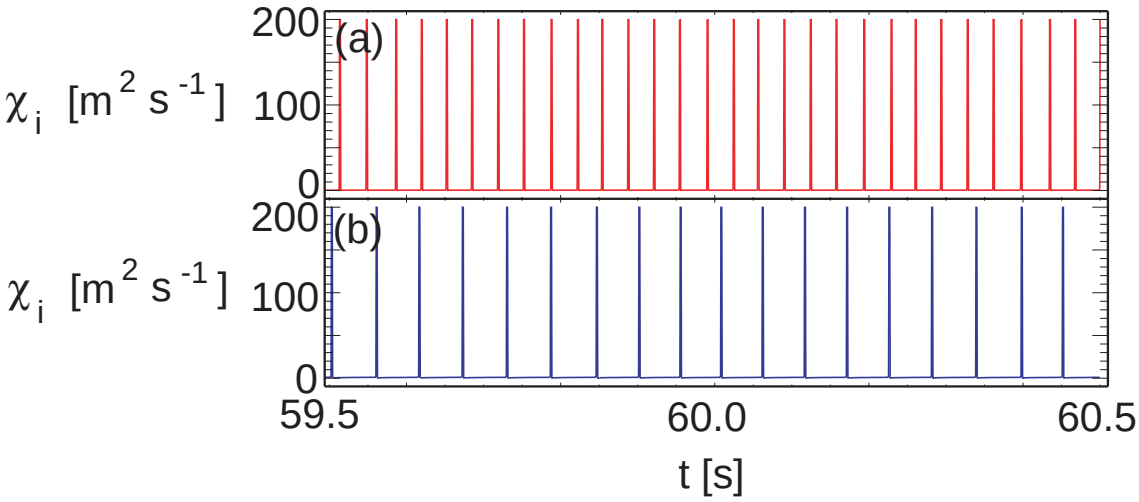

Figure 3.2: *Ion thermal conductivity as a function of time at the magnetic surface* $\rho = 0.97$ *in two typical JETTO simulations with an* ad hoc *model for type I ELMy H-mode with different levels of external heating power. (a)* $P = 16$ MW*, (b)* $P = 8$ MW.

3.1.3 Susceptibility for Type II ELMs

Publication 2 also discusses various conditions reported to be favourable for the occurrence of type II ELMs and seeks to explain such proneness to type II ELMy H-mode in terms of the MHD stability assumptions described above. Among the conditions and features reported to increase the susceptibility for type II ELMs are strong neutral gas puffing [81], a quasi double null magnetic configuration [82, 83], i.e. a magnetic configuration featuring proximity to a second singularity over and above the usual singularity used to shape the field lines in the vicinity of the divertor, high poloidal β [84], high edge safety factor q_{95} [85, 86] and high triangularity δ [85, 86]. By performing MHD stability analysis with MISHKA-1 on interpretative JETTO runs, it is shown in Publication 2 that each of these conditions tends to make the outermost plasma edge more unstable against infinite-n ballooning modes, in other words make the plasma more susceptible to type II ELMs according to the interpretation explained above.

3.2 Transition from Type I to Type III ELMy H-Mode

From experiments, it is known that plasma easily accommodates modest external neutral gas puffing, e.g. a neutral influx of 3×10^{22} s^{-1} in the case of JET. Higher

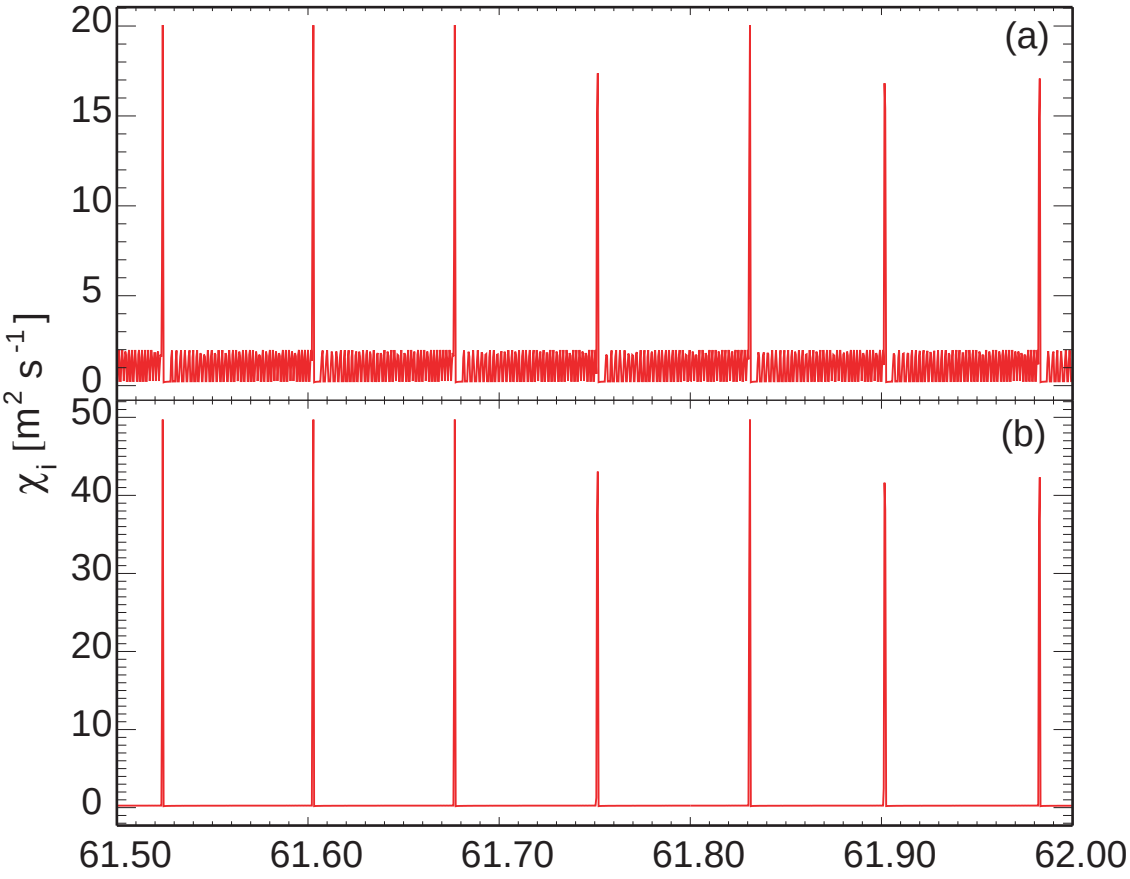

Figure 3.3: *Ion thermal conductivity as a function of time in a typical JETTO simulation with an* ad hoc *model for mixed type I-II ELMy H-mode at (a)* $\rho = 0.995$*, (b)* $\rho = 0.965$*.*

levels of gas puffing can trigger a transition from type I to type III ELMs with a dramatic increase in the ELM frequency followed by a deterioration of plasma confinement. [81]

In Publication 1, it is shown that strong external neutral gas puffing can cause a sequence of causalities involving the edge density, collisionality, bootstrap current, total edge current and magnetic shear, eventually triggering a transition from second to first ballooning stability. Initially, the level of neutral influx across the separatrix for a few different levels of external neutral gas fuelling has been established in simulations with the integrated transport code COCONUT. Because of ionization in the SOL, only a small fraction of the total gas puff actually penetrates the separatrix and enters the confined plasma. In fact, the neutral influx across the separatrix turns out to be between one and two orders of magnitude smaller than the applied puff rate. The effect on separatrix density and temperature has then been studied in the simulations with COCONUT. Due to ionization of neutrals, increased neutral gas puffing increases the density in the edge plasma. Given that the pressure gradient

and thus the pressure cannot increase uncontrollably, the temperature decreases. It should be noted that evaluating the neutral influx across the separatrix and the density and temperature evolution in response to it in a self-consistent way requires a tool like COCONUT with the capability to simulate the entire plasma in an integrated fashion.

The sequence of causalities resulting from an increase in the level of external neutral gas puffing has been explored further with the JETTO core transport code using the self-consistent separatrix density and temperatures calculated by COCONUT as boundary conditions. In the JETTO runs, collisionality at the edge increases with the increasing edge density resulting from an increase in external neutral gas puffing. To a first approximation, the bootstrap current I_{bs} scales as $I_{bs} \sim 1/(1+\nu^*)$, where ν^* is the collisionality. As a result of the increased collisionality at the edge, there is a significant decrease of the bootstrap current with increasing gas puffing. Doubling the puff rate nearly halves the bootstrap current in some parts of the parameter range. Hence, the edge current, which comprises to a larger extent of bootstrap current but also of Ohmic current, decreases by a similar amount. Magnetic shear increases with decreasing edge current, roughly in inverse proportions to the edge current density in some parts of the parameter space.

It is known that magnetic shear controls MHD stability in general and infinite-n ballooning stability in particular. MHD stability analysis with the codes HELENA and MISHKA-1 shows that when the effect is strong enough, increased magnetic shear due to external neutral gas fuelling can cause a transition from second to first ballooning stability, in other words a transition from the situation in frame (a) in Fig. 3.1 to the situation in frame (b).

It is clear that the critical pressure gradient decreases abruptly by a factor of about two during the transition from second to first ballooning stability. In the work described in Publication 1, making the assumption that stability is controlled entirely by the pressure gradient limit, the effect on the ELM frequency of the transition has been modelled with JETTO. The *ad hoc* ELM model for type I ELMs described in Sec. 3.1 has been used. As expected, the ELM frequency increases dramatically in the simulations, when the critical pressure gradient drops by a factor of two. The increase in the ELM frequency is accompanied by a deterioration of plasma confinement, which follows from the fact that a smaller pedestal pressure gradient leads to a lower pedestal height and due to profile stiffness also to lower core pressure. The behaviour resembles the experimentally observed transition from type I to type III ELMs triggered by an increase in the external neutral gas fuelling. Therefore, it can be concluded that, qualitatively, the transition from second to first ballooning stability resembles the experimentally observed transition from type I to type III ELMy H-mode with the concomitant increase in ELM frequency and deterioration of plasma confinement.

Finally, it is worth noting that the preceding discussion also provides a good example of what can be achieved through integrated predictive modelling and why it is needed. The final conclusion has been reached through a process involving integrated modelling of the entire plasma, stand-alone modelling of the confined plasma, MHD stability analysis and the use of a simplistic ELM modelling scheme.

3.3 Modelling with Theory-Motivated ELM Models

Given the importance of the ELM phenomenon, it is clear that it is desirable to have more sophisticated models for it than the very crude *ad hoc* models discussed in the previous subsections. For this reason, models based on linear ballooning and peeling mode stability theory have been developed, as discussed in Publications 3 and 4. Publication 3 introduces a minimal model for describing the linear evolution of the ballooning mode amplitude. The ELMs are represented by exponentially growing fluctuations in a simple linear MHD model for a system with a background thermal noise. The idea here is to improve upon the *ad hoc* ELM modelling scheme introduced in Sec. 3.1 by calculating the ELM amplitude and ELM duration from a model based on theoretical considerations rather than assigning these parameters in an *ad hoc* fashion. This can most readily be achieved by introducing an equation for the time-evolution of the ballooning mode amplitude and scaling transport in the ELM-affected area according to this calculated mode amplitude. The general form of such an equation can quite easily be deduced from the general properties of MHD instabilities. To begin with, in ideal MHD the growth rate of the mode should be zero below a stability threshold defined in terms of a critical pressure gradient in the case of a ballooning mode. When above the stability threshold, the mode amplitude should grow at the characteristic growth rate of a ballooning mode. In addition to a growth rate term, one can also conceive of a damping rate term due to non-ideal MHD effects that tries to return the mode amplitude back to the level of thermal noise. Finally, the equation should account for the fact that due to toroidal coupling between the individual harmonics making up a ballooning mode, such modes are global, i.e. localized over a finite region of the edge plasma rather than confined to specific magnetic surfaces.

Based on these considerations, the following linear differential equation has been constructed for the ballooning mode amplitude:

$$\frac{d\xi}{dt} = \frac{1}{N} \sum_{k\,=\,k_{\text{top of ETB}}}^{k_{\text{separatrix}}} \left[C_1 \frac{c_{s,k}}{\sqrt{L_{p,k} R_k}} \left(1 - \frac{\alpha_c}{\alpha_k}\right) H\left(1 - \frac{\alpha_c}{\alpha_k}\right) \xi - C_2 \frac{c_{s,k}}{R_k} \left(\xi - \xi_0\right) \right]. \tag{3.1}$$

Here, the index k runs over mesh points, $N = k_{\text{separatrix}} - k_{\text{top of ETB}}$ is the number of mesh points within the ETB, $C_1 \sim 1$, $C_2 \sim 0.1$ and $\xi_0 \sim 0.01$ are constants characterizing the growth rate of the instability, the decay rate of the mode due to

non-ideal MHD effects and the level of background fluctuations, respectively, H is the Heaviside function defined as $H(x) = 0$, if $x < 0$ and $H(x) = 1$, if $x \geq 0$, x being an arbitrary variable, $c_s = \sqrt{T_e/m_i}$ is the sound speed, $L_p = p/|dp/dr|$ is the pressure scale length, r is the minor radius, R is the major radius and α_c is the critical normalized pressure gradient.

The coefficients C_1, C_2 and ξ_0 have been chosen so that a regime of discrete oscillations is obtained. The choice of the coefficients C_1 and C_2 so that $C_1 \sim 1$ and $C_2 \ll C_1$ goes in line with what would be expected from a general description of the ballooning mode instability. Specifically, the choice $C_1 \sim 1$ corresponds to the typical growth rate of a ballooning mode [87] and the choice $C_2 \sim 0.1$ to a gyro-Bohm diffusion time for a mode the radial scale of which is a few ion gyro-radii. The choice $\xi_0 \sim 0.01$ is just a description of the background thermal noise level. As Publication 4 mentions, the behaviour of the model is somewhat insensitive to the values of C_1, C_2 and ξ_0, once the model has entered a regime of discrete oscillations.

Above the threshold α_c, the mode amplitude increases linearly with a growth rate equal to the ballooning mode growth rate. The factor $c_s/\sqrt{L_p R}$ corresponds to the ballooning mode growth rate well above the instability threshold. Below the threshold α_c, the growth rate is zero due to the Heaviside function, which is a way of taking into account the fact that there is no damping or growing solution in ideal MHD with $\alpha < \alpha_c$ and of reproducing the transition from an oscillating solution to a growing solution taking place when the critical pressure gradient is exceeded. The second term inside the brackets on the right-hand side of Eq. (3.1) describes the level of background fluctuations and the decay rate of the mode after an ELM crash due to non-ideal MHD effects such as finite viscosity and diffusivity, and causes the mode amplitude to tend to converge towards the level of background fluctuations between the ELMs. The coefficient $C_2 c_s/R$ determines the rate at which the mode is damped after an ELM crash.

The sum in Eq. (3.1) runs over all mesh points within the ETB. Averaging Eq. (3.1) over the ETB is a way of accounting for the global nature of ballooning modes. The assumption that the radial extent of the unstable mode usually coincides with the ETB width has been crosschecked in numerical analysis with the ideal linear MHD stability code MISHKA-1 [88].

At each time step, the (normalized) pressure gradient, pressure scale length and temperature calculated by JETTO are used to evaluate the perturbation amplitude ξ, and Gaussian-shaped transport perturbations having amplitudes proportional to the perturbation amplitude ξ given by Eq. (3.1) are added on top of the radial profiles of the transport coefficients within the ETB and its vicinity. Specifically,

the additional transport perturbation $\delta\chi$ representing ELMs can be written

$$\delta\chi(r,t) \sim \xi(t) \exp\left[-\left(\frac{r-r_0}{\Delta}\right)^2\right], \tag{3.2}$$

where r_0 is the radial location of the centre of the Gaussian and Δ is the characteristic width of the Gaussian. In this way, the ELM modelling scheme interacts with the transport simulation through a feedback loop working in both directions.

The use of Gaussian-shaped ELMs is motivated by the fact that the ballooning modes assumed to drive the ELMs have Gaussian shapes in linear theory. The parameters r_0 and Δ are determined on a case-by-case basis by analysing the structure of the unstable modes in the type of plasma being modelled. The transport perturbation is usually assumed to coincide with the eigenfunction of the most unstable mode. In most cases, the ELM-affected area roughly coincides with the pedestal.

The fact that the perturbations applied to the transport coefficients scale linearly with the calculated ballooning mode amplitude is consistent with the commonly used quasi-linear approximation [89]. Arguably, the enhancement of the transport coefficients should scale with the ballooning mode amplitude as something in the range from almost no dependence, consistent with the constant saturated level of diffusivity in the strong turbulence limit, to the quadratic dependence given by the quasi-linear approximation. The linear dependence used here lies in between these two extremes and gives qualitatively the same results as the quadratic dependence.

In Publication 3, it is demonstrated that the linear ballooning model described by Eq. (3.1) produces discrete oscillations when coupled to a transport simulation and that it can qualitatively reproduce the dynamics of type I ELMy H-mode, including an ELM frequency that increases with increasing external heating power. Like the simpler *ad hoc* models introduced in Sec. 3.1, the theory-motivated ballooning model lacks the full predictive capability of reproducing the exact time of onset, duration and amplitude of each individual ELM, but it improves upon the simpler models in the sense that it gives qualitatively the correct behaviour in a wide range of situations with a minimum number of free parameters.

Publication 3 further discusses the conditions necessary for obtaining discrete oscillations and the ELM generation mechanism. Generally, several conditions have to be fulfilled in order to obtain discrete oscillations with a model like Eq. (3.1). Usually, the model has to be at least one-dimensional, i.e. no oscillations are obtained in a zero-dimensional system. It is essential that the model is coupled to a transport simulation, as here. It also seems to be necessary that the ELMs are represented by perturbations with a finite width, e.g. by using Gaussian-shaped eigenfunctions as here. In addition, the averaging over the whole pedestal and the discretization provided by the Heaviside function seem to be of some importance.

In Publication 3, it is demonstrated that apart from these factors the onset of discrete oscillations is related to how the radial profiles of the transport coefficients are perturbed in the transport simulation and to how the pressure gradient evolves as a result of this.

3.4 Modelling with a Theory-Motivated Ballooning-Peeling ELM Model

3.4.1 Theory-Motivated Ballooning-Peeling ELM Model

As discussed earlier, a broadly held view is that ELMs can be triggered both by ballooning modes controlled mainly by the edge pressure gradient and by peeling modes driven mainly by the edge current. An apparent deficiency of the model described by Eq. (3.1) is that it takes into account ballooning mode stability only, or to put it differently, makes the assumption that the ELMs are controlled by ballooning mode stability only. An obvious improvement would be to relax this assumption. It should be stressed, nevertheless, that the simplifying assumption that stability is controlled by ballooning modes only is still often a valid assumption.

Publication 4 describes how the theory-motivated ballooning model described by Eq. (3.1) has been extended to take into account peeling modes: In this case two mutually analogous linear differential equations, one for ballooning modes and one for peeling modes, are solved separately and the mode amplitudes from each equation are added up to give a total mode amplitude:

$$\frac{d\xi_b}{dt} = \frac{1}{N} \sum_{k\,=\,k_{\text{top of ETB}}}^{k_{\text{separatrix}}} \left[C_b \gamma_{b,k} \left(1 - \frac{\alpha_c}{\alpha_k} \right) H\left(\alpha_k - \alpha_c\right) \xi_b - C_d \frac{c_{s,k}}{R_k} \left(\xi_b - \xi_0\right) \right] \tag{3.3}$$

$$\frac{d\xi_p}{dt} = \frac{1}{N} \sum_{k\,=\,k_{\text{top of ETB}}}^{k_{\text{separatrix}}} \left[C_p \gamma_{p,k} \left(1 - \frac{J_{c,k}}{J_k} \right) H\left(J_k - J_{c,k}\right) \xi_p - C_d \frac{c_{s,k}}{R_k} \left(\xi_p - \xi_0\right) \right] \tag{3.4}$$

$$\xi = \xi_b + \xi_p \tag{3.5}$$

Here, γ_p is the peeling mode growth rate. Generally, $\gamma_b = \gamma_p = c_s/\sqrt{L_p R}$ has been used, i.e. the ballooning and peeling mode growth rates have for simplicity been assumed equal. The simplification $\gamma_p = \gamma_b$ can be used, because the model has been shown to be relatively insensitive to the growth rates. For peeling stability, a localized stability criterion based on the MHD energy principle is used. The condition for peeling stability, omitting the mesh point indices, is $J < J_c$, where the quantities J and J_c, which are used analogously to the pressure gradient and

the critical pressure gradient in the equations for the mode amplitude, are defined as [33]:

$$J = 1 + \frac{1}{\pi q'} \oint \frac{j_{\parallel} B}{R^2 B_{\theta}^3} dl - \Delta_v \tag{3.6}$$

$$J_c = \sqrt{1 - 4D_M}, \tag{3.7}$$

Here, D_M is the Mercier index [90, 91], which is proportional to the pressure gradient p', q' is the gradient of the safety factor, $j_{\parallel}$ is the current density parallel to the magnetic field, B is the magnetic field strength and Δ_v is a vacuum energy parameter describing the distance from the external surface to the plasma surface.

3.4.2 Combined Ballooning-Peeling ELMs

Like the theory-motivated ballooning model, the combined ballooning-peeling model reproduces the experimental dynamics of type I ELMy H-mode, including an ELM frequency that increases with power, when coupled to a JETTO transport simulation. It has been demonstrated that the individual ELMs are usually driven by a combination of ballooning and peeling modes. Figure 3.4, which shows the time evolution of some plasma parameters during a typical combined ballooning-peeling ELM, gives some insight into the dynamics of such an ELM. The data used in the figure is from a simulation using the magnetic equilibrium of a JET high-triangularity ELMy H-mode plasma, pulse number 53298. Frame (a) shows the ion thermal conductivity at the magnetic surface $\rho = 0.92$ of maximum ELM amplitude, frame (b) the global ballooning mode growth rate $\overline{\gamma}_B = \sum_k [C_b \gamma_{p,k} (1 - \alpha_c/\alpha_k) H(\alpha_k - \alpha_c)]/N$ and frame (c) the global peeling mode growth rate $\overline{\gamma}_P = \sum_k [C_p \gamma_{b,k} (1 - J_{c,k}/J_k) H(J_k - J_{c,k})]/N$. Frames (d) – (h) show time traces of a number of plasma parameters at six different magnetic surfaces, namely $\rho = 0.94$, $\rho = 0.95$, $\rho = 0.96$, $\rho = 0.97$, $\rho = 0.98$ and $\rho = 0.99$. Specifically, frame (d) shows time traces of the normalized pressure gradient α, frame (e) of the total current parallel to the magnetic field $j_{\parallel}$, frame (f) of the expression J_c (Eq. (3.7)) in the peeling mode stability criterion, frame (g) of the expression J (Eq. (3.6)) in the peeling mode stability criterion and frame (h) of the expression $J - J_c$. The dotted line in frame (d) indicates the critical pressure gradient.

It should be noted that a very large-amplitude and long-duration ELM has deliberately been chosen for Fig. 3.4 in order to make the behaviour of the parameters illustrated more clearly visible. For purposes of studying the behaviour of the model, the scaling of the transport enhancement in response to the calculated mode amplitude can be varied. The ELM size and duration can also to some extent be varied by adjusting the parameters C_1, C_2 and ξ_0. As is the case with the simpler models introduced earlier in this chapter, it is difficult to reproduce the actual experimental ELM times, durations and amplitudes with the combined ballooning-peeling model

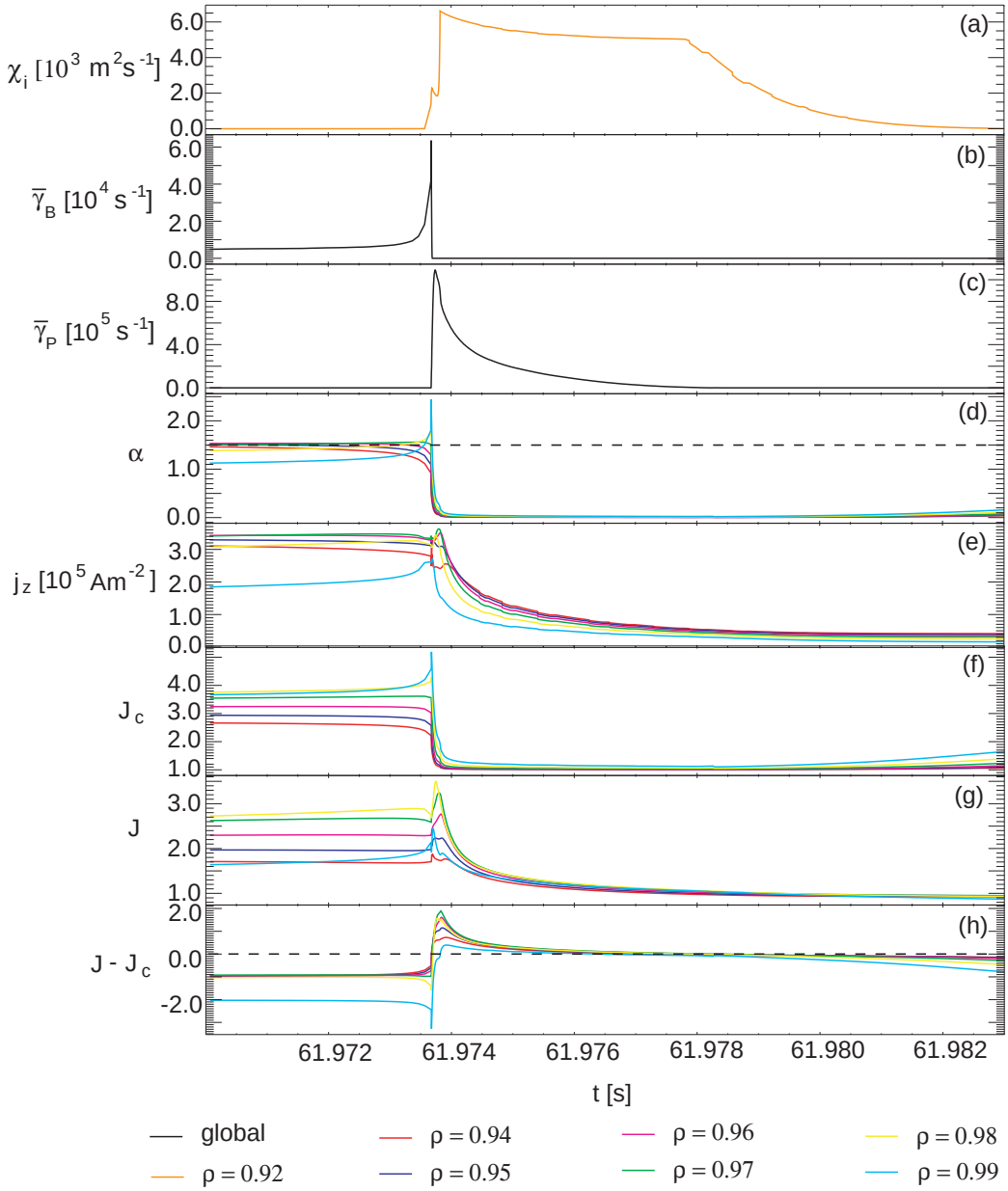

Figure 3.4: *Time traces of a number of parameters of interest in a simulation with the combined ballooning-peeling ELM model defined by Eqs. (3.3) – (3.5): (a) ion thermal conductivity χ_i, (b) global ballooning mode growth rate $\overline{\gamma}_B$, (c) global peeling mode growth rate $\overline{\gamma}_P$, (d) normalized pressure gradient α, (e) toroidal current density $j_\parallel$, (f) the threshold J_c in the peeling mode stability criterion $J < J_c$, (g) the expression J in the peeling stability criterion, (h) the expression $J - J_c$. The ion thermal conductivity in frame (a) has been plotted at the radial location of the maximum ELM amplitude, whereas the quantities in frames (d) – (h) have been plotted at six different magnetic surfaces: $\rho = 0.94$, $\rho = 0.95$, $\rho = 0.96$, $\rho = 0.97$, $\rho = 0.98$ and $\rho = 0.99$.*

defined by Eqs. (3.3) – (3.5), given the exceedingly complex nature of the ELM phenomenon.

By comparing the time traces of the ion thermal conductivity, the global ballooning mode growth rate and the global peeling mode growth rate in Fig. 3.4, it becomes clear that the ELM starts as a ballooning mode instability and continues as a peeling mode instability. It should, however, be noted that the critical pressure gradient is exceeded and the global ballooning mode growth rate becomes finite already long before the discrete peak in the growth rate develops. The complete ballooning phase is thus remarkably lengthy in comparison to the visible high-amplitude phase of the ELM during which the transport coefficients rise to levels significant enough to have a tangible effect on say the plasma profiles.

As shown in frame (d) in Fig. 3.4, the ballooning component of the ELM eventually becomes so strong that it starts to deplete the pressure gradient at the edge, whereby α quickly falls below the critical level and the ballooning mode instability fades away. The edge current, however, reacts more slowly to the onset of the ELM, as shown in frame (e) in Fig. 3.4. This is a direct consequence of the general property that the current evolves more slowly than the pressure gradient. Since the Mercier coefficient scales as $D_M \sim p'$ and generally $D_M < 0$, the stability threshold J_c given by Eq. (3.7) decreases in phase with α, as illustrated in frame (f) in Fig. 3.4. Because the current responds to the transport enhancement induced by the ballooning phase of the ELM more slowly than the pressure gradient, the quantity J given by Eq. (3.6) does not decrease but even increases slightly during the initial fast drop in J_c. Hence, the peeling stability criterion $J < J_c$ is violated during the collapse of α induced by the ballooning phase of the ELM. This becomes very evident by looking at the time trace of $J - J_c$ in frame (h) in Fig. 3.4. The expression $J - J_c$ exceeds zero when the initial drop in the pressure gradient occurs. At the onset of the ELM, the plasma is still deeply peeling stable.

Because of the slow redistribution of the current, it takes a comparatively long time for the ELM to reduce J given by Eq. (3.6) to a level below the stability threshold J_c. Therefore, the peeling phase of the discrete ELM peak lasts noticeably longer than the brief large-amplitude phase of ballooning instability preceding it. The feature that the decay time of the ELM is of the order of or longer than both the peak ballooning phase and the peeling phase of the ELM is due to the fact that the damping rate term in Eqs. (3.3) – (3.4) is much smaller than the ballooning and peeling mode growth rate terms, as determined by the choices $C_d \ll C_b$ and $C_d \ll C_p$.

Fig. 3.5 shows the typical ballooning-peeling mode ELM cycle in an (α, $j_\parallel$) operational space. The figure shows a trace made up of points of equidistant temporal separation. Due to the fact that the redistribution of the edge current is generally much slower than evolution of the edge pressure gradient, the combined ballooning-

peeling mode ELMs are triggered by a violation of the ballooning stability criterion. The collapse of the pressure gradient induced by the ballooning phase of the ELM then leads to a violation of the peeling mode stability criterion and the ELM continues in a generally lengthy peeling mode phase until the edge current density has been depleted to a stable level. It should be noted that the ELM cycle obtained here resembles the cycle for type I ELMs predicted in Ref. [39].

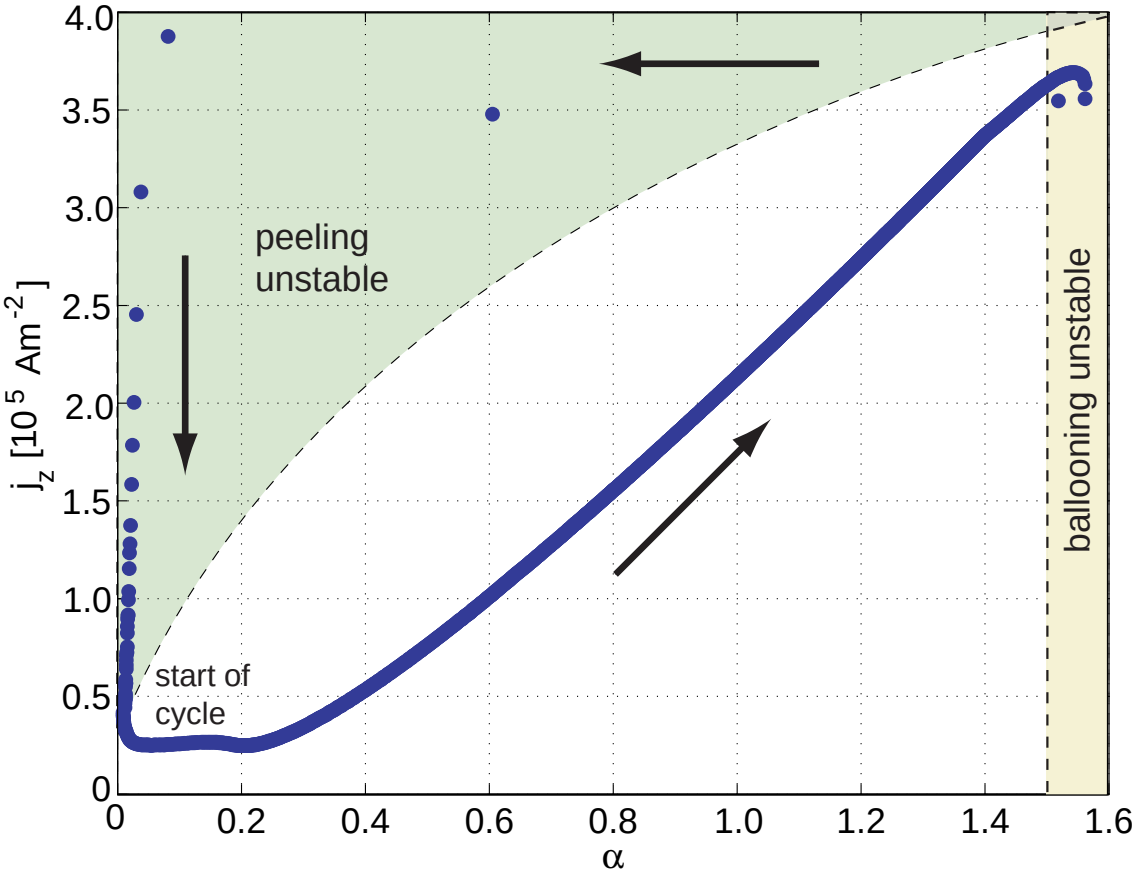

Figure 3.5: *The path traced in the α-$j_\parallel$ operational space at the magnetic surface $\rho = 0.99$ during one ELM cycle in a simulation with the combined ballooning-peeling ELM model described by Eqs. (3.3) – (3.5). Consecutive points in the trace are equidistant in time. The approximate locations of the ballooning and peeling mode unstable domains have been indicated.*

Even though the model produces combined ballooning-peeling ELMs triggered by a ballooning mode instability in most circumstances, it sometimes yields pure ballooning ELMs or pure peeling ELMs. Pure peeling ELMs are often obtained during current ramp-ups and pure ballooning ELMs during current ramp-downs.

Like the theory-motivated ballooning model introduced in Sec. 3.3, the combined ballooning-peeling model lacks the full predictive capability of quantitatively reproducing the actual times of onset, durations and amplitudes of individual ELMs.

Qualitatively, however, the combined ballooning-peeling model improves significantly on the ballooning model by taking into account the dynamics of peeling modes.

3.5 Effects of Ripple-Induced Thermal Ion Losses on H-Mode Plasma Performance

Much effort has been put into understanding and predicting the intricacy of how confinement and ELM properties depend on various plasma parameters, heating power, machine size and various other parameters, which has led to the development of various scaling laws e.g. for the energy confinement time [92–94]. These scaling laws give an expression for the desired quantity, say the energy confinement time, as a function of parameters such as plasma current, toroidal magnetic field, average density, external heating power, machine size and plasma shape, and can be used to predict confinement in future devices such as ITER. An interesting application is to test such dependencies in identity experiments involving two or more tokamaks. Starting from 2004, a series of such identity experiments has been carried out at JET and the Japanese JT-60U tokamak by a team with personnel from both machines [51].

In many respects, the JT-60U tokamak is a machine similar to JET. In terms of physical size, in particular, the two tokamaks feature rather similar parameters, with JT-60U having an only 10% larger major radius than JET. A major difference is, however, that JT-60U features only 18 toroidal field coils in comparison to 32 at JET, as a result of which the level of toroidal magnetic field ripple is significantly higher in the former machine, despite ferritic inserts carefully designed to reduce it.

In the JET / JT-60U dimensionless pedestal identity experiments, a good match between the two tokamaks was obtained in all the main dimensionless plasma parameters: the normalized plasma pressure β, the normalized gyro-radius ρ^* and the collisionality ν^*. A special JT-60U-like equilibrium was developed at JET in order to match the plasma shape of JT-60U in terms of the triangularity δ and elongation κ. The dimensionless identity technique makes use of the invariance of plasma physics to changes in the dimensional plasma parameters. Given the fact that the similar sizes of JET and JT-60U makes it possible to carry out such dimensionless pedestal identity experiments with nearly identical dimensional plasma parameters, the experiments were regarded as particularly interesting.

Despite the good match in dimensionless parameters, the pedestal identity experiments failed, contrary to expectations, to produce plasmas with similar dimensional pedestal parameters. Specifically, the ELM frequency is generally lower and

the pedestal performance better in JET discharges than in their JT-60U identity matches [51].

Publication 5 summarizes the analysis performed to explain the discrepancies observed in pedestal performance and ELM frequency in the series of dimensionless pedestal identity experiments at JET and JT-60U. As a result of thorough analysis, it was concluded that the MHD stability of the pedestal is rather similar in both machines and that the observed discrepancies cannot be explained by differences in the MHD stability of the pedestal. The explicit dependence of the MHD stability of the pedestal on the aspect ratio was investigated, because JT-60U features a 10% smaller inverse aspect ratio than JET. It was shown that MHD stability depends very little on the aspect ratio. The fact that plasmas from the two machines feature rather different toroidal plasma rotation profiles — JET plasmas co-rotate, i.e. rotate in the direction of the toroidal magnetic field, whereas JT-60U plasmas counter-rotate and generally feature a lower rotation velocity — was also taken explicitly into account. It was concluded that toroidal rotation affects the MHD stability of the pedestal very modestly. Some studies on other machines have indicated that plasma rotation may have a non-negligible effect on the MHD stability of the pedestal [95], but in the JET/JT-60U dimensionless pedestal identity plasmas the effect on marginal stability was only of the order of a few percent.

The failure to explain the results of the dimensionless pedestal identity experiments at JET and JT-60U with differences in the MHD stability of the pedestal triggered an effort to explore the role of ripple-induced transport in these experiments. The rationale for exploring the effect of ripple losses was the fact that JT-60U features a high level of toroidal magnetic field ripple in comparison to JET. It was realized that thermal ion losses due to ripple transport have been relatively unexplored, perhaps due to associations with L-mode transport. In the L-mode, contrary to the state of things in the H-mode, all transport coefficients have relatively large values in the region just inside the separatrix, in comparison to which any ripple-induced additional transport is small in magnitude, whereby any effects due to the ripple field remain hidden.

After these initial conclusions, the remainder of Publication 5 then describes the results of predictive transport modelling of the effects of ripple losses of thermal ions on H-mode plasma performance. The analysis makes use of results from orbit-following simulations performed with the Monte Carlo orbit-following code ASCOT by Finnish co-workers on relevant JET and JT-60U equilibria. ASCOT has been run using a "pulse spreading" technique, in which the transport coefficients are measured from the variance growth of an initially radially localized test particle ensemble with a Maxwellian velocity distribution defined by the local temperature [96]. The simulations indicate that both losses due to diffusive transport and non-diffusive (direct) losses can give rise to transport significantly exceeding the level of ion neoclassical transport and thus be important in H-mode discharges. Losses due to

diffusive transport have been shown to give rise to a broad radial distribution of ion thermal conductivity, whereas non-diffusive losses have been demonstrated to be very edge-localized. In the following two subsections, the effects of each type of losses on plasma performance and ELM characteristics are analysed in turn, using the JETTO transport code for predictive transport simulations. For modelling of ELMs, the *ad hoc* model for type I ELMs described in Sec. 3.1 has been used in the simulations.

3.5.1 Modelling of Plasma with Non-Diffusive Losses

As Publication 5 describes, the JETTO transport code has been equipped with suitable models for ripple-induced transport, which have been used in combination with the *ad hoc* model for type I ELMs and the *ad hoc* ETB model. For non-diffusive losses of thermal ions, a simple *ad hoc* model commonly referred to as the τ-approximation has been used. In this approach, a convective energy sink term $-\nu n_i T_i$ is added to the continuity equation for the ion pressure:

$$\frac{\partial(n_i T_i)}{\partial t} = P - \nabla(\chi_i n_i \nabla T_i) - \frac{n_i T_i}{\tau_{ripple}}. \tag{3.8}$$

Here, P is the power density, and $\tau_{ripple}(\rho) = 1/\nu(\rho)$ is the characteristic edge confinement time, which decreases strongly towards the separatrix due to non-diffusive losses, and ν is the characteristic ion escape rate due to non-diffusive losses. It should be noted that only very deeply trapped ions are susceptible to direct ripple losses. The characteristic ion escape rate ν effectively takes into account how the deeply trapped part of the velocity space is filled up by collisions.

Figures 3.6 – 3.8 illustrate the characteristic results obtained with the model for non-diffusive losses. Two simulations are used in each figure, one reference simulation with no non-diffusive losses and another one with a maximum loss rate of 100 s^{-1}. Figure 3.6 compares the ion escape rate profiles in the two simulations, one of which corresponds to the situation with no losses. The edge-localized ion escape rate profile with a maximum loss rate of 100 s^{-1} in the other simulation roughly corresponds to the loss rate profile obtained in the ASCOT simulation for the relevant scenario. Figure 3.7, which shows the pressure profiles in the two simulations at times shortly before ELMs, illustrates the effect on plasma performance. A straightforward comparison of the two graphs reveals that there is a discernible flattening of the pressure profile just inside the separatrix in the simulation with modelling of non-diffusive losses included, which results in an effective narrowing of the pedestal. Given that the achievable pedestal pressure gradient remains the same in the two cases, the loss of plasma just inside the separatrix leads to a lower top-of-the-pedestal pressure. Due to profile stiffness, the lower top-of-the-pedestal pressure of the effectively narrower pedestal translates into lower pressure throughout the core plasma and thus into reduced confinement.

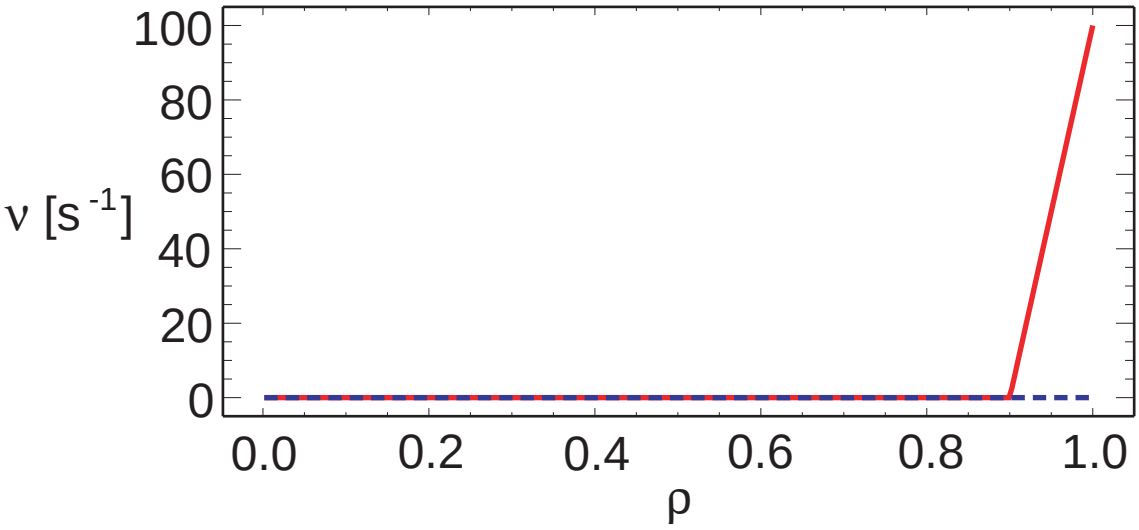

Figure 3.6: *Radial profiles of the imposed ion escape rate in a simulation with the τ-approximation model for non-diffusive losses (solid curve) and in a reference simulation with no imposed losses (dashed curve).*

A further illustration of the effect on plasma performance is given in Fig. 3.8, which shows time traces of the thermal energy content and a measure known as confinement factor H-89 [92] for the two simulations. The H-89 confinement factor, which has been time-averaged over the ELM cycles in Fig. 3.8, is based on a scaling law and is a measure of the quality of the H-mode. The thermal energy content and confinement factor decrease with increasing non-diffusive losses in accordance with the levels of plasma pressure in Fig. 3.7. The effect on the ELM frequency is visible in the time traces of the thermal energy content in Fig. 3.8. The ELM frequency increases with increasing non-diffusive losses mainly because the ELM size in terms of particle and energy loss drops due to the effective narrowing of the pedestal. With the effectively narrower pedestal and thus lower pedestal height, each ELM modelled by an increase in transport from the separatrix up to the top of the pedestal removes less energy and particles. The smaller ELM size in terms of particle and energy loss for unchanged ELM amplitude and ELM duration with the introduction of non-diffusive losses is evident in Fig. 3.8. As a result of the smaller ELM energy and particle losses, the recovery from each ELMs is faster, whereby the ELM frequency goes up. A second less important reason for the higher ELM frequency with the introduction of non-diffusive losses is increased transport inside the pedestal. This follows from profile-stiffness-like behaviour of the Bohm transport model in response to the lower pedestal height.

The reduced plasma confinement and increased ELM frequency obtained in the simulations with non-diffusive losses resemble the results obtained at JT-60U in the dimensionless pedestal identity experiments with JET. This suggests that non-diffusive losses associated with the stronger magnetic ripple at JT-60U might explain

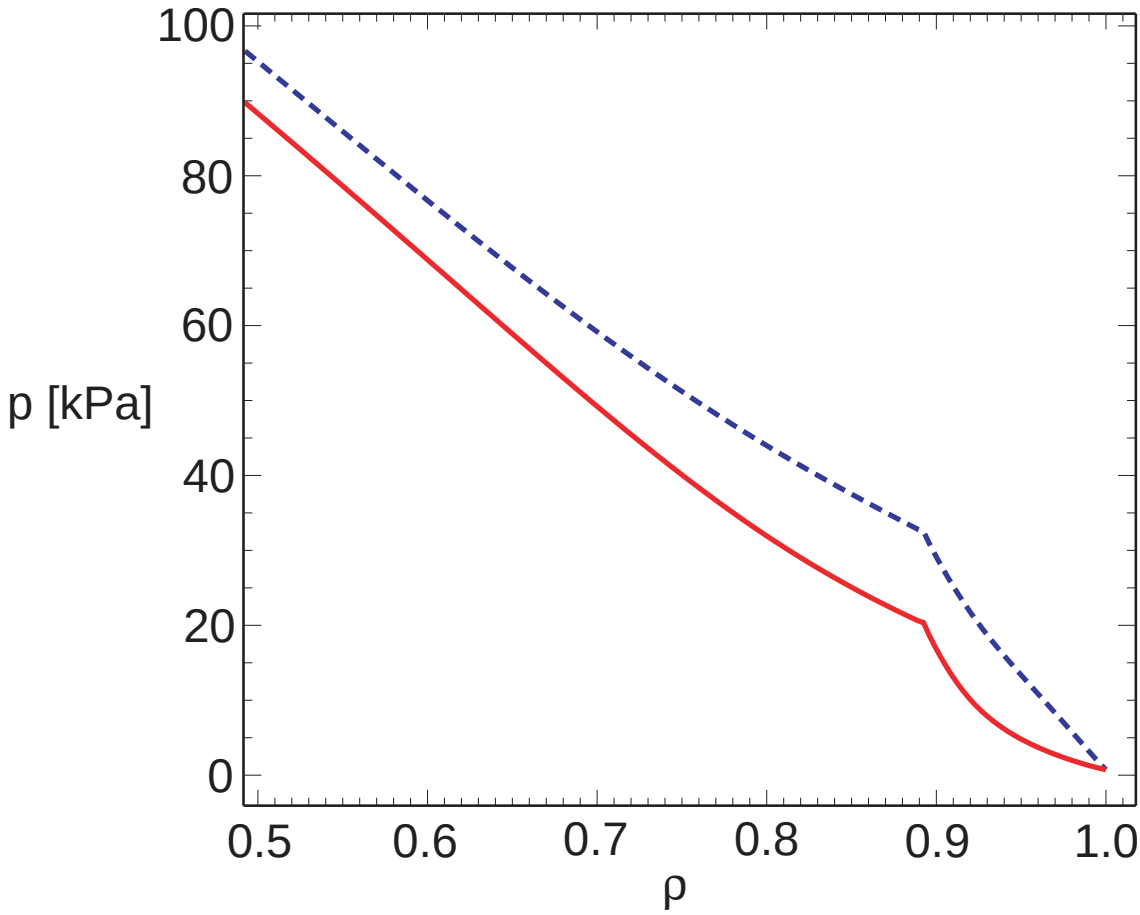

Figure 3.7: *Radial profiles of the total pressure at times shortly before ELMs in the simulation with the τ-approximation model for non-diffusive losses (solid curve) and in the reference simulation with no losses (dashed curve).*

the modest pedestal performance and high ELM frequency observed in this machine. It should, however, be kept in mind that in a real plasma the ELM amplitude and duration, which are fixed in the *ad hoc* ELM model used here, may of course also be affected by ripple losses. The modelling does not take this into account, but the effects are probably not significant enough to affect the qualitative trends revealed here. Finally, it should also be remembered that the pedestal width has been kept fixed. A possible inward movement of the top of the pedestal might weaken the tendency towards reduced confinement and higher ELM frequency observed in the simulations, but it is speculative at best whether ripple losses could at all have such an effect on the pedestal structure.

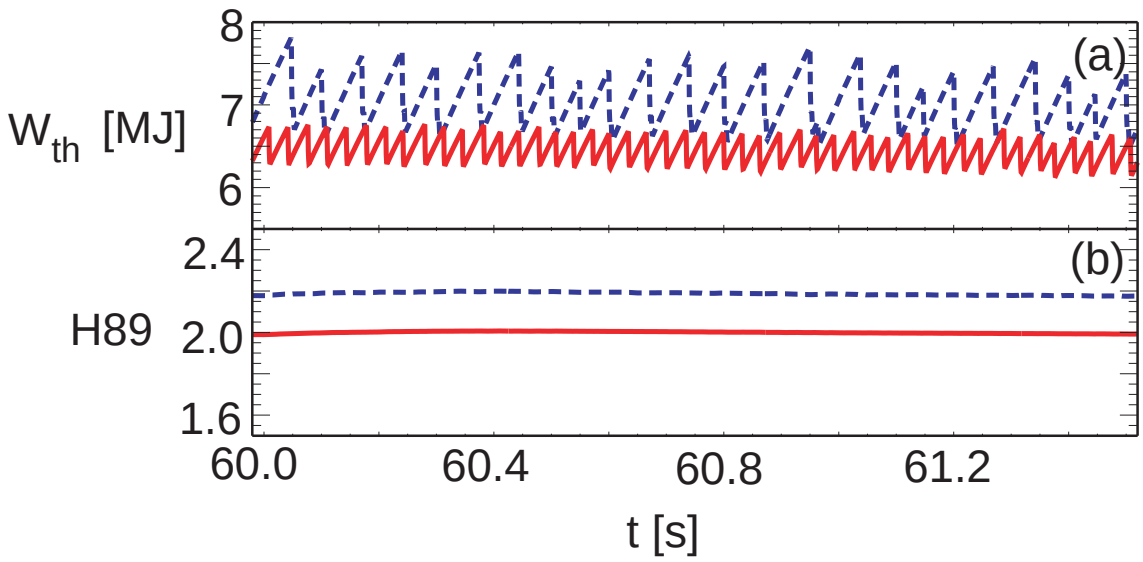

Figure 3.8: *(a) Thermal energy content and (b) confinement factor H-89 time-averaged over the ELM cycles as a function of time in the simulation with the τ-approximation model for non-diffusive losses (solid curve) and in the reference simulation with no losses (dashed curve).*

3.5.2 Modelling of Plasma with Losses due to Diffusive Transport

For losses due to diffusive transport, a simple analytical approximation [48] for ripple-induced ion thermal conductivity adjusted according to the results obtained with ASCOT has been used. In accordance with the orbit-following calculations, the ion thermal conductivity representing the ripple-induced contribution has a characteristic width significantly wider than the pedestal width. Figures 3.9 – 3.13 illustrate a set of results obtained with this assumption. The radial profile of inter-ELM ion thermal conductivity used in the simulation is shown in Fig. 3.9 together with the profile from a reference simulation without additional transport. As required, the transport perturbation is significant in amplitude well beyond the top of the pedestal in comparison with the ion neo-classical level of ion thermal conductivity within the ETB. Given the drop in background ion thermal conductivity at the top of the pedestal, this leads to the structure with two distinct peaks for the total ion thermal conductivity. The characteristic shape of the ion thermal conductivity profile in the core plasma follows from the Bohm/gyro-Bohm transport model and varies somewhat over time.

The effect on the ELM frequency of introducing the transport perturbation is demonstrated in Fig. 3.10, which shows the ion thermal conductivity at the magnetic surface $\rho = 0.95$ as a function of time. In this case, the ELM frequency decreases

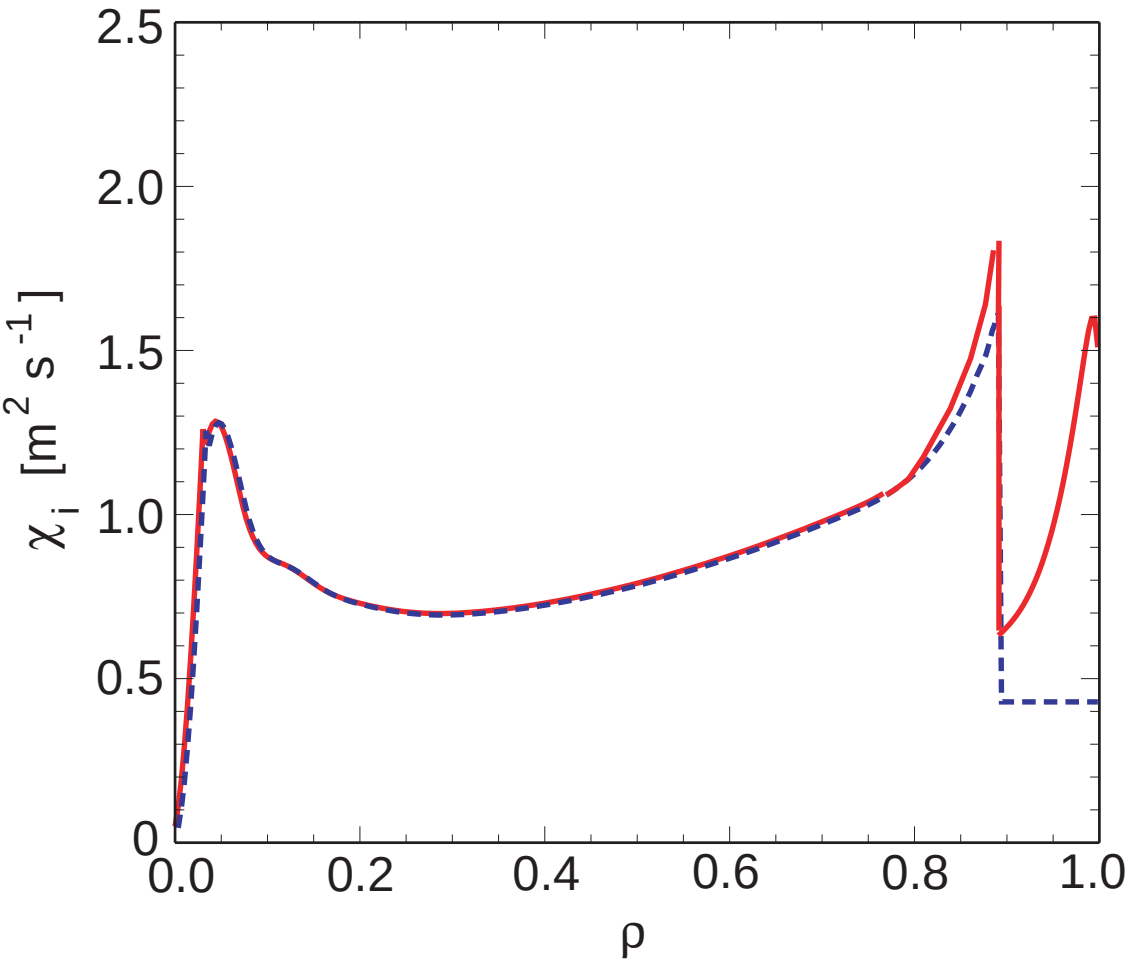

Figure 3.9: *Radial profiles of ion thermal conductivity in two predictive transport simulations without (dashed curve) and with (solid curve) a contribution representing ripple-induced ion thermal transport at the edge. A broad radial profile consistent with ASCOT simulations is assumed for the contribution representing ripple-induced transport.*

appreciably with the introduction of additional transport at the edge. The explanation for this is that the increased transport at the edge leads to increased losses between the ELMs and thus to a longer ELM build-up time. Here, this effect is the dominating mechanism affecting the ELM frequency. For clarity, it should be mentioned that a similar tendency towards a lower ELM frequency is of course also present in the modelling of plasma with non-diffusive losses discussed in the preceding subsection, but there the mechanisms working towards a higher ELM frequency are much stronger and dominate the situation.

As a result of the lower ELM frequency with the introduction of ripple-induced transport, the time-average top-of-the-pedestal temperature increases considerably,

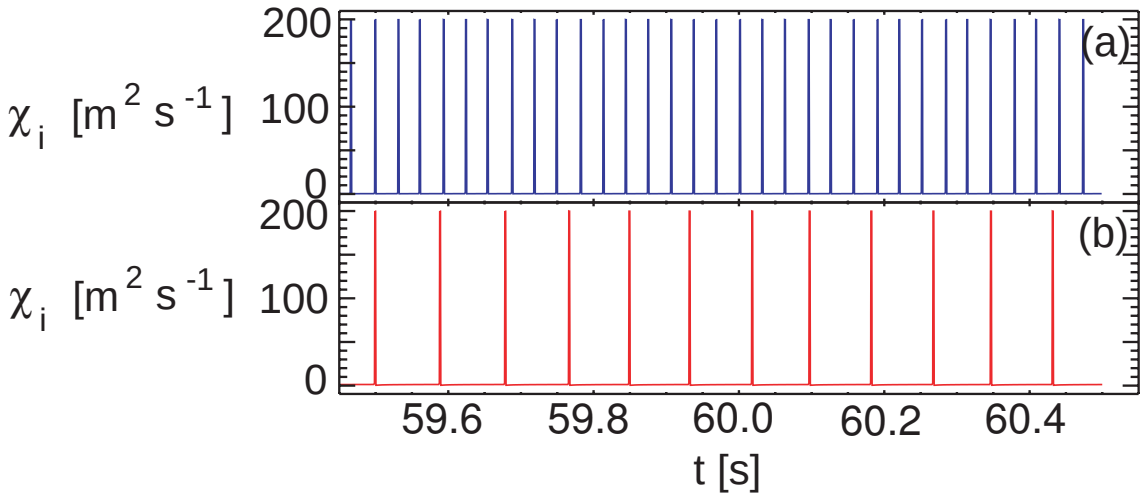

Figure 3.10: *Ion thermal conductivity at* $\rho = 0.95$ *as a function of time in the two predictive transport simulations used in Fig. 3.9. (a) No contribution representing ripple-induced transport. (b) Ripple-induced transport included.*

even though the ultimate pre-ELM pedestal height does not change. The time-average temperature at the top of the pedestal is larger for slower pedestal build-up, because the temperature generally increases most rapidly for a relatively constant amount of time right after an ELM crash and then saturates more and more slowly over time before the next ELM. This is illustrated in Fig. 3.11, which shows the ion and electron temperatures at the top of the pedestal as a function of time for the duration of the longer of the two ELM cycles in the simulations with and without additional ion thermal conductivity representing ripple-induced transport. It is evident that the time average of the ion and electron temperatures is higher in the case with the lower ELM frequency. As a practical demonstration of this effect one can also think of the limiting case of a conceivable ELM-free H-mode, in which the pressure gradient would saturate at a value just below the critical pressure gradient. In the absence of ELMs, the temperature at the top of the pedestal would settle at a constant level almost as high as the pre-ELM temperature in an ELMy H-mode with the same critical pressure gradient. Clearly, the constant top-of-the pedestal temperature in the ELM-free H-mode would be higher than the time-average top-of-the-pedestal temperature in the ELMy H-mode.

The effect on plasma performance becomes evident in Fig. 3.12, which shows the pressure profiles in the simulations at times shortly before ELMs. The maximum pressure at the top of the pedestal is the same in the two cases, but since the lower ELM frequency in the simulation with ripple-induced transport leads to higher time-average top-of-the-pedestal temperature and thus to higher time-average top-of-the-pedestal pressure, the core pressure becomes higher in this case due to profile stiffness. In this way, ripple-induced additional ion thermal transport at the edge

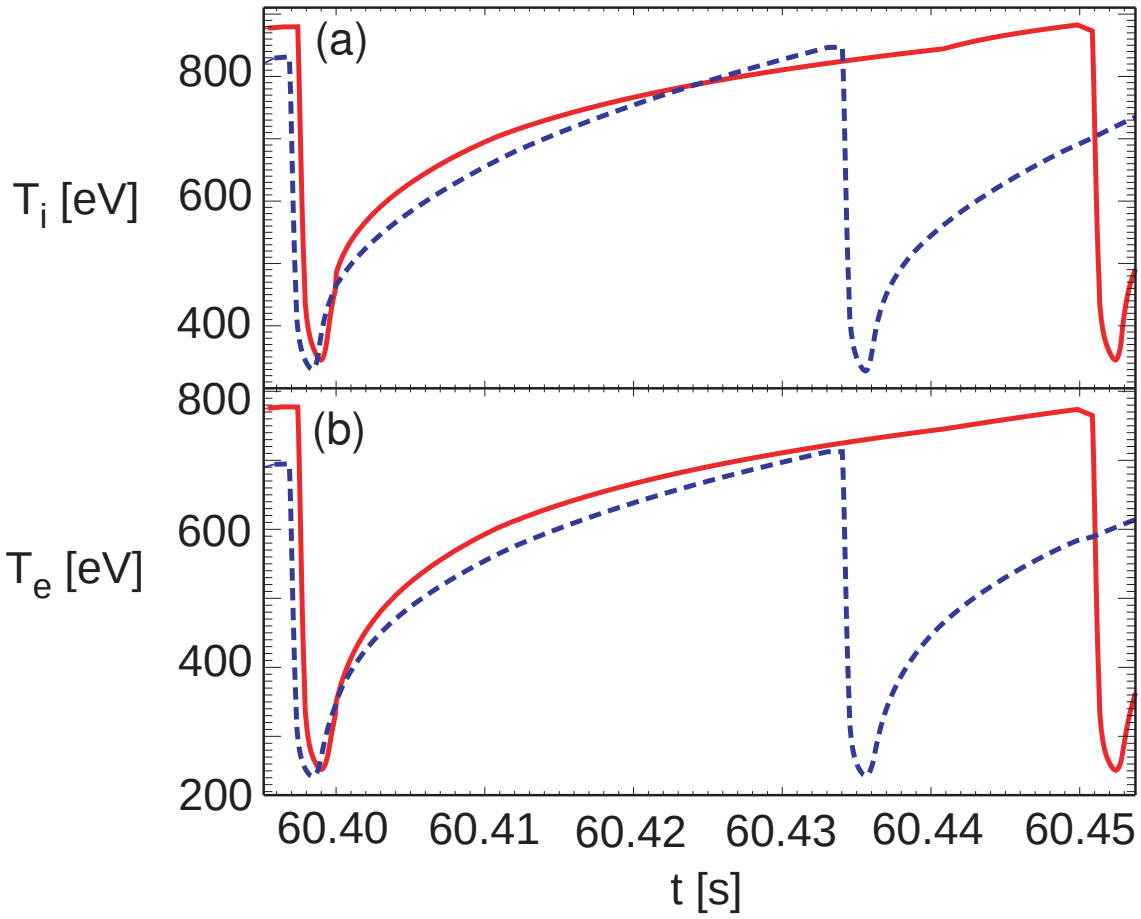

Figure 3.11: *(a) Ion temperature and (b) electron temperature at the top of the pedestal as a function of time for the duration of the longer of the two ELM cycles in the two predictive transport simulations used in Fig. 3.9. Dashed curve: no contribution representing ripple-induced transport. Solid curve: ripple-induced transport included.*

can lead to improved overall confinement. A further illustration of the improved performance resulting from the ripple-induced additional ion thermal conductivity is given in Fig. 3.13, which compares the thermal energy content and confinement factor H-89, time-averaged over the ELM cycles, in the two simulations.

Generally ripple losses have been associated with a detrimental influence on confinement. It should be noted, however, that there are, in fact, some experimental indications of improved performance in the presence of ripple losses, as one might expect from the modelling results. In particular, the improved performance demonstrated

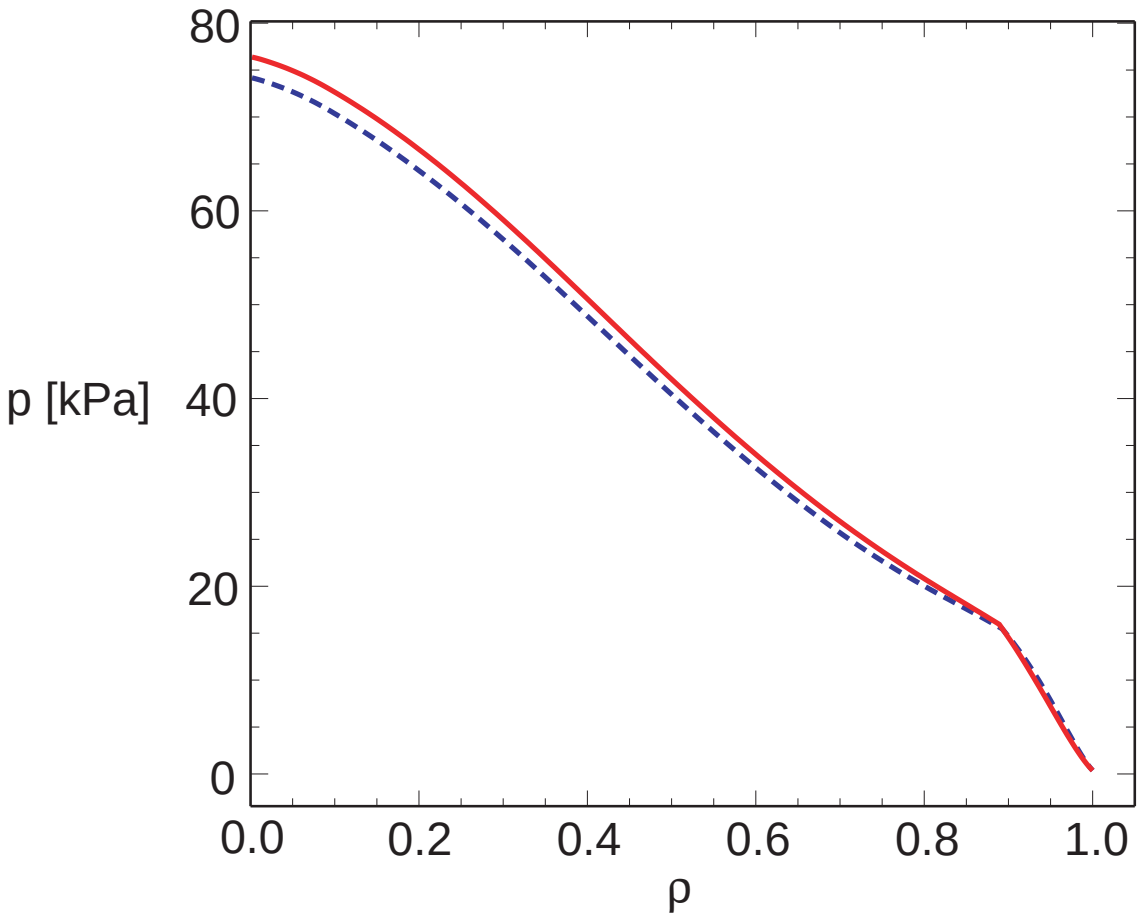

Figure 3.12: *Radial profiles of the total pressure at times shortly before ELMs in the two predictive transport simulations used in Fig. 3.9. Dashed curve: no contribution representing ripple-induced transport. Solid curve: ripple-induced transport included.*

in the simulations qualitatively resembles a slight improvement in confinement obtained with small ripple amplitudes in previous JET experiments [97]. Reduced performance in the presence of ripple losses, as in the recent JET / JT-60U dimensionless pedestal identity experiments, nevertheless, seems to be a more common result. One possible inference of this is that the non-diffusive losses are comparatively stronger than the losses due to diffusive transport in JT-60U, making the tendency towards reduced performance the dominating effect. As discussed in Publication 5, a more edge-localized profile of additional ion thermal transport following from losses due to diffusive transport would also result in a tendency towards reduced performance and more benign ELMs, i.e. qualitatively the same result as with non-diffusive losses in Sec. 3.5.1. Such a narrow profile of enhanced transport has, however, not been seen in the orbit following simulations.

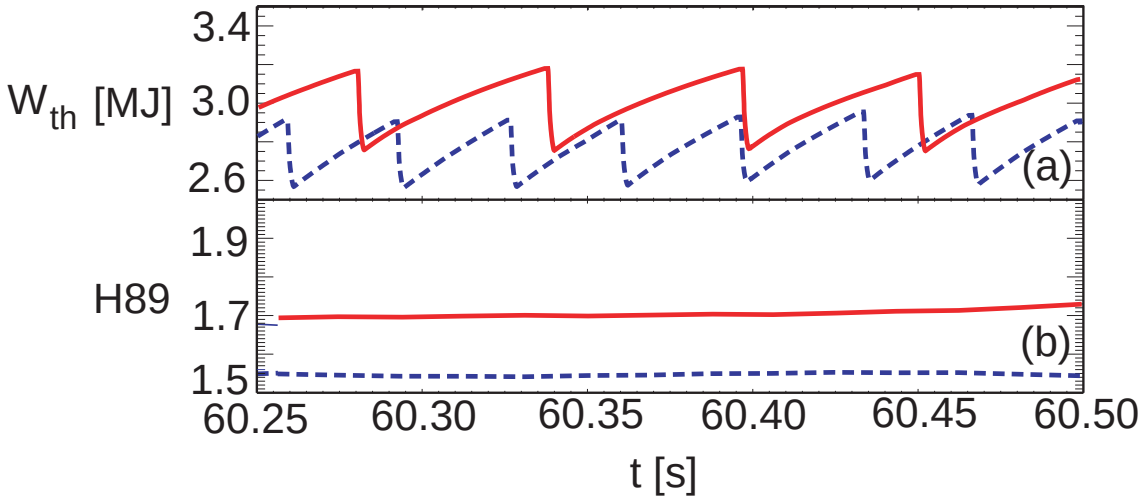

Figure 3.13: *(a) Thermal energy content and (b) confinement factor H-89 time-averaged over the ELM cycles as a function of time in the two predictive transport simulations used in Fig. 3.9. Dashed curve: no contribution representing ripple-induced transport. Solid curve: ripple-induced transport included.*

It should also be kept in mind that as in the modelling of plasma with non-diffusive losses the ELM amplitude has been kept fixed in the modelling described in the present subsection, given that the focus has been on qualitative trends only. The tendency towards improved pedestal performance and less frequent ELMs may be reduced or strengthened, if the ELM amplitude is allowed to change in response to the introduction of ripple losses. Such an effect cannot be modelled with the *ad hoc* ELM model used here. The overall tendency towards improved performance and less frequent ELMs is, nevertheless, likely to be the dominant effect in any case, because the ELM amplitude needs to drop significantly before the ELMs actually start to get more frequent. It should also be noted that a reduced ELM frequency, as obtained here, most often leads to larger, more violent ELMs.

The result obtained with losses due to diffusive transport is interesting, because it shows that ripple losses need not necessarily have a detrimental influence on performance. On the contrary, improved confinement may be obtained by carefully tailoring the ripple amplitude profile. The modelling also indicates that there is a trade-off between confinement and the benignity of ELMs, so that improved performance leads to more violent ELMs and vice versa.

Above all, the modelling of the effects of ripple losses also demonstrates how sensitively even small levels of additional transport due to ripple losses may affect the physics of the H-mode pedestal. The results may have widely felt implications, in particular because ITER is foreseen to operate with a level of ripple higher than that at JET despite making use of ferritic inserts designed to reduce the inhomogeneity

of the toroidal field. Indeed, a formal effort to investigate the effects of ripple losses in the ITER tokamak has recently been launched as a matter of urgency.

It should also be noted that qualitatively similar results to those with toroidal magnetic field ripple can probably be obtained by edge ergodization using an externally induced resonant magnetic perturbation, as some studies already indicate [98]. Toroidal magnetic field ripple, which affects ion transport, and edge ergodization, which affects electron transport, can in many respects be seen as complementary techniques.

3.6 ELM Heat Pulse Propagation in the Scrape-off Layer

Albeit much of the work discussed in this thesis has focused on the physics of the H-mode pedestal in situations without the explicit need to consider the SOL, some scenarios have also been studied in which integrated modelling of the whole plasma including the SOL is essential for the self-consistency of the results. In such work, the integrated transport code COCONUT has been used. Publication 6 deals with one of the key physics topics studied in this way: the propagation of an ELM-induced heat pulse from the outer midplane of the tokamak towards the divertor targets.

In this work, a heat pulse has been induced at the outer midplane of a high-density plasma by increasing the perpendicular transport coefficients in the ETB and SOL. In the ETB on the 1D JETTO grid, perpendicular transport has been increased radially uniformly by a factor of the order of 100 relative to the inter-ELM ion neoclassical level. In the SOL on the 2D EDGE2D grid, the perpendicular transport enhancement has been distributed poloidally according to a narrow Gaussian distribution (typically with a half width of $\pi/16$ in terms of poloidal angle) centred at the outer midplane. At the separatrix, the poloidal average of the Gaussian distribution has been set to match the level of transport in the ETB.

In some initial simulations, the poloidally Gaussian-shaped distribution of perpendicular transport during the ELM was extended radially uniformly throughout the SOL. With this distribution of transport in the SOL, the radial transport across the field lines is noticeably fast compared to the parallel transport along the field lines. Not surprisingly, it was seen that this leads to an enormous heat flux at the wall, something which has not been seen in experiments. Clearly, the distribution of perpendicular transport should decrease across the SOL.

Ramping down perpendicular transport across the SOL towards the outer edge of the simulation grid removes the heat flux to the wall and most of the power thus

flows to the divertor targets, as appropriate. Somewhat surprisingly, however, it was found that with no heat flux to the wall and the parallel transport given by the 21-moment approximation the ion heat flux at the divertor targets turns out to be much smaller than the electron heat flux. It is demonstrated in Publication 6 that the reason for this discrepancy is strong ion-electron equipartition, i.e. a transfer of energy from the ions to the electrons.

Further simulations show that the ion-electron equipartition varies strongly as a function of the plasma parameters. The higher the density, the larger a fraction of the total energy carried by the ions is transferred to the electrons. This is illustrated in Fig. 3.14, which shows time integrals of the total ion heat flux measured at both targets, the total electron heat flux measured at both targets and the volume-integrated ion-electron equipartition energy as a function of time for three simulations with different densities. Frame (a) in Fig. 3.14 corresponds to a simulation with an average separatrix density of 8×10^{18} m^{-3}, frame (b) to a simulation with an average separatrix density of 1.7×10^{19} m^{-3} and frame (c) to a simulation with an average separatrix density of 4.0×10^{19} m^{-3}. The sequence of figures clearly shows how the amount of energy carried by the ions relative to that carried by the electrons decreases as the ion-electron equipartition energy increases with the density.

The fact that the experimentally observed ion and electron heat fluxes at the targets are not straightforward to reproduce suggests that parallel transport is important. Figure 3.15 shows how the ion and electron heat fluxes at the outer and inner targets vary with different assumptions for the heat flux limiting factors. Four different levels of the heat flux limiting factors have been used: $\alpha_{flux,\,i} = \alpha_{flux,\,e} = 0.2$, $\alpha_{flux,\,i} = \alpha_{flux,\,e} = 1.0$, $\alpha_{flux,\,i} = \alpha_{flux,\,e} = 2.0$ and $\alpha_{flux,\,i} = \alpha_{flux,\,e} = 3.0$. The figure reveals a couple of interesting facts: Firstly, it should be noted that the divertor asymmetry of a larger total heat flux to the inner target than to the outer target clearly visible in the figure is consistent with experimental measurements at the JET and ASDEX Upgrade tokamaks [99]. Secondly, it should be observed that especially the ion heat fluxes vary significantly as a function of the flux limiting factors and that about $\alpha_{flux,\,i} = \alpha_{flux,\,e} = 1.0$ is needed for a significant response to be seen at the outer target and about $\alpha_{flux,\,i} = \alpha_{flux,\,e} = 2.0$ for a sizable response at the inner target. The considerable sensitivity of the result on the heat flux limiting factors unambiguously demonstrates that the fluid approach alone, which cannot determine the heat flux limiting factors self-consistently, is insufficient for accurately modelling transients. The obvious conclusion is that, instead, the heat flux limiting expressions have to be calculated kinetically during transients. Such work has already been undertaken [100], which paves the way for an integrated fluid-kinetic approach in future work.

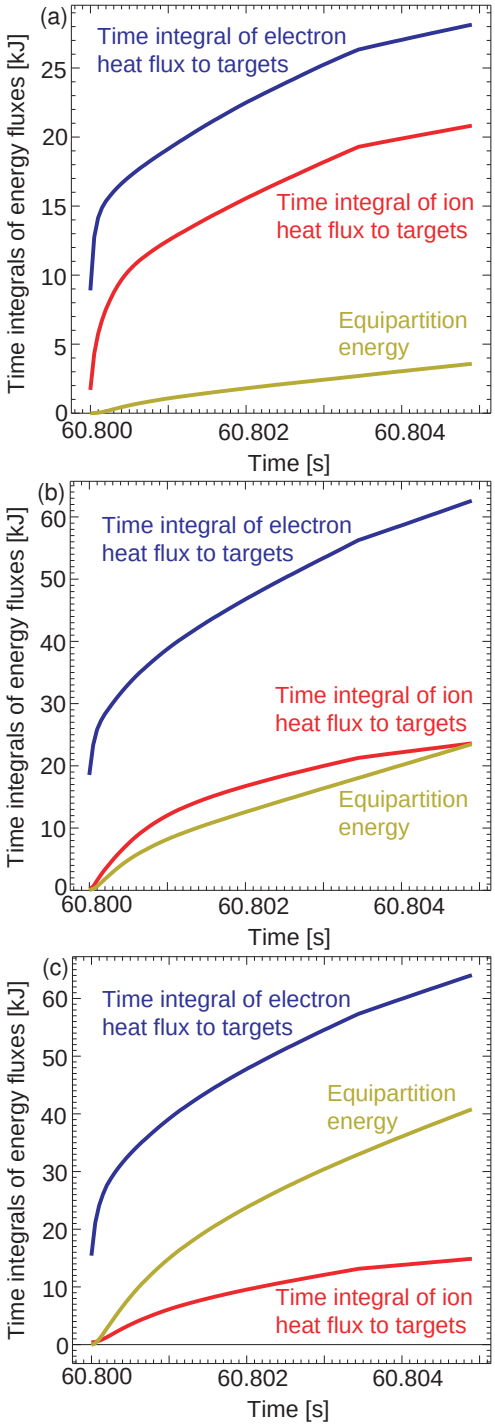

Figure 3.14: *Time integrals of the total ion heat flux measured at the targets, the total electron heat flux measured at the targets and the volume-integrated ion-electron equipartition energy as a function of time for three COCONUT ELM simulations with the following separatrix densities: (a)* 8×10^{18} m^{-3}*, (b)* 1.7×10^{19} m^{-3} *and (c)* 4×10^{19} m^{-3}.

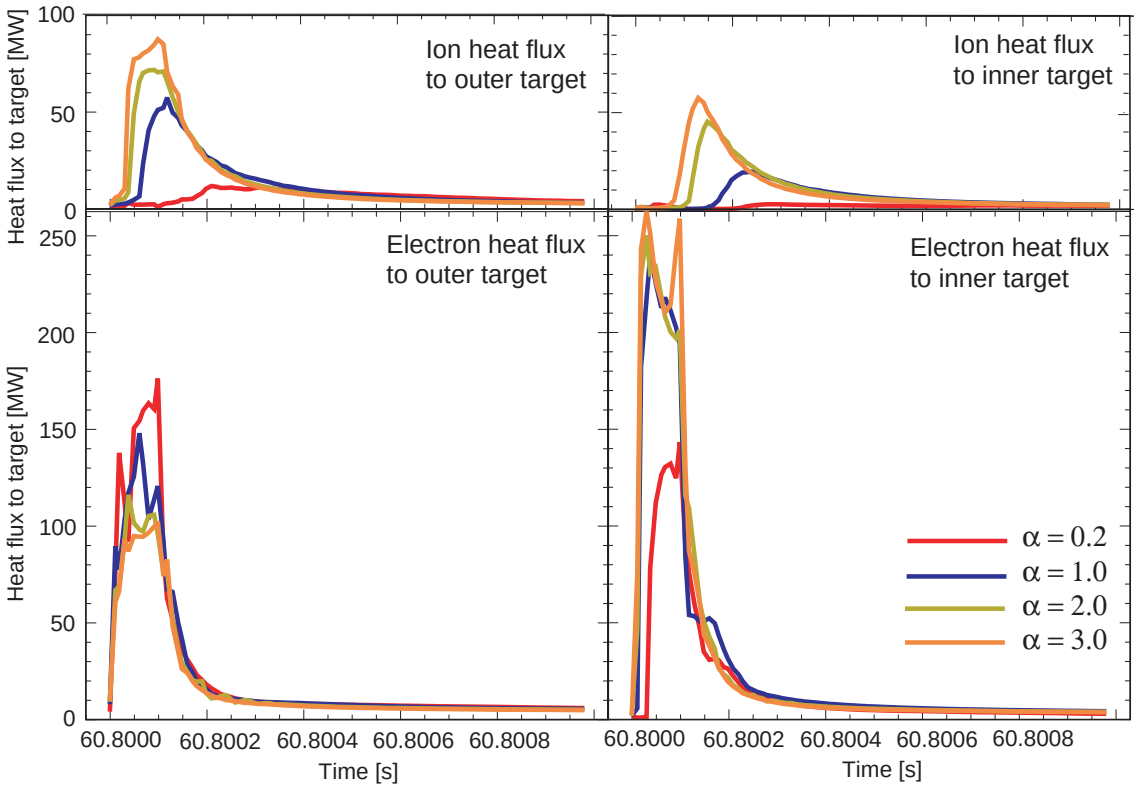

Figure 3.15: *Ion and electron heat fluxes at the outer and inner targets for four different values of the parallel heat flux limiting factors in ELM simulations with COCONUT.*

Chapter 4

Summary and Discussion

Understanding the intricate physics of the plasma edge in a tokamak is crucial when it comes to designing devices compatible with the requirements of commercial reactor operation. Based on the present knowledge of tokamak design, one can say that the edge plasma plays a dual role in controlling tokamak operation: Firstly, the formation of an edge transport barrier with enhanced transport characteristics just inside the magnetic separatrix in H-mode plasmas is paramount to achieving a level of confinement sufficient for an adequate fusion burn to be sustained. Thanks to a phenomenon known as profile stiffness, improved performance in the edge pedestal translates into a higher level of performance throughout the core plasma. Secondly, the edge plasma in H-mode discharges is prone to generating ELMs, which in addition to limiting confinement cause severe heat loads on the divertor target plates and other first wall components. Mitigating the ELMs and designing a reactor vessel able to sustain the ELM power loads for extended periods of time are, without exaggeration, principal challenges on the tortuous path towards commercialization of fusion energy. Indeed, owing to the fact that relying on the ELMy H-mode inherently leads to pulsed operation of the tokamak in combination with extreme periodic heat loads, advanced tokamak scenarios relying entirely on non-inductive current drive may eventually become the preferred mode of operation of commercial fusion reactors.

This thesis describes a systematic research effort aimed at improving the understanding of the physics of the plasma edge and exploring ways of controlling the performance of the pedestal and reducing the impact of the ELMs. Much of the work has been done by means of studying plasma transport, how plasma plasma transport is modified by various effects and how various effects can be described and explained in terms of modification of plasma transport. Given that the transport properties determine how quickly the plasma loses energy and particles, plasma transport also directly determines the level of confinement. Moreover, the ELM phe-

nomenon has often been interpreted as resulting from a modification of transport driven by MHD instabilities. It should be noted, however, that alternative explanations to this mainstream view have been proposed as well [101, 102].

The first part of the work describes various ELM models used in 1D transport modelling. It has been shown that even very crude *ad hoc* models are capable of qualitatively reproducing the experimental dynamics of type I ELMy H-mode and can be highly useful in qualitative studies of various effects. In a quantitative sense these models have no predictive capability, however, because quantities such as the ELM amplitude, ELM duration and ELM-affected area are set arbitrarily. Some predictability of the ELM frequency can, nevertheless, be achieved by adjusting the ELM size in such a way that each ELM removes the experimentally measured amount of particles and energy. Subsequently, more sophisticated ELM models with fewer free parameters have been introduced. In these models, the ELM amplitude and ELM duration are calculated self-consistently from a simple model of instability. Even these models have a limited predictive capability, however. They do not predict the ELM frequency very well and nor do they predict the sizes of individual ELMs. This is because the models are still rather crude simplifications of a phenomenon so complex that it is not fully understood. Nevertheless, the models are able to predict qualitative trends like changes in the ELM frequency and ELM size, the dynamics of the ELM cycle and perhaps even the susceptibility for different ELM types. In particular, simulations with a theory-motivated combined ballooning-peeling model seem to indicate that ELMs are often driven by a combination of ballooning and peeling modes. Such combined ballooning-peeling ELMs are most often triggered by a ballooning mode instability, which by reducing the pressure gradient renders the plasma peeling mode unstable, given that the current redistribution occurs considerably more slowly than the pressure gradient collapse. As a result of this, the ELM continues in a lengthy peeling mode phase, which lasts until current redistribution renders the plasma stable again.

A major recent application in which the *ad hoc* ELM models have been used for qualitative study has been the modelling of the effects of ripple-induced thermal ion losses in H-mode plasmas described in Sec. 3.5. Given that ITER even with the installation of ferritic inserts designed to reduce the inhomogeneity of the magnetic field will feature a level of toroidal magnetic field ripple considerably higher than JET and that recent experiments and modelling indicate that this, contrary to the previously held view, is a non-negligible issue, investigating the effects of ripple losses has received considerable attention recently. The work on ripple losses presented in this thesis, however, was initiated already prior to these realizations owing to the fact that no other effects seemed to be able to explain the results of a series of dimensionless pedestal identity experiments at JET and JT-60U, in which there was a considerable discrepancy between the two machines in terms of plasma performance and ELM frequency.

Based on orbit-following simulations with the Monte Carlo orbit-following code ASCOT, predictive transport simulations of scenarios with both losses due to diffusive transport and non-diffusive ripple losses were set up. The orbit-following simulations indicate that both types of losses can be important and, furthermore, that non-diffusive losses tend to be very edge-localized, whereas losses due to diffusive transport result in noticeable additional ion thermal transport well beyond the top of the pedestal.

Encouragingly, predictive transport modelling with JETTO making use of a simple model for non-diffusive losses reproduces the JT-60U results. It has been demonstrated that the highly edge-localized non-diffusive losses lead to an effective narrowing of the pedestal by removing plasma particles from the layer just inside the separatrix, and therefore to a lower pedestal height, which through profile stiffness translates into lower core pressure and thus into reduced confinement. Thanks to the reduced energy content following from the lower pedestal height, the ELM size decreases, at least with the assumptions of the simple *ad hoc* model for ELMs used in the study. As a result of this, the ELM recovery time decreases, despite a weaker tendency of the increased edge losses to lead to a longer ELM recovery time, and the ELM frequency, consequently, increases. A tempting conclusion is that non-diffusive ripple losses at JT-60U lead to the reduced performance and more frequent and benign ELMs in this machine in comparison to JET. Apart from that, it seems obvious that ELM mitigation techniques based on magnetic ripple could be devised and perfected.

Interestingly, the opposite result with improved performance and less frequent, presumably more dangerous ELMs is obtained, if one makes the assumption of a profile of enhanced transport consistent with that obtained for losses due to diffusive transport in the orbit-following simulations. In this case, the tendency of the enhanced losses at the edge to lead to a longer ELM build-up time is the dominating effect, whereby the ELM frequency decreases. The longer ELM recovery time results in a higher average top-of-the-pedestal temperature and thus in higher average top-of-the-pedestal pressure, which through profile stiffness translates into improved overall performance. Incidentally, a behaviour resembling this qualitatively was observed in a series of experiments with enhanced ripple at JET in 1995 for small ripple amplitudes.

In addition to providing a plausible explanation for the striking difference in plasma performance and ELM properties between JET and JT-60U in dimensionless pedestal identity experiments between the two machines, the modelling implies that there is a trade-off between performance and benignity of ELMs, so that improved performance comes at the expense of more violent ELMs and vice versa. The results may have sizable and widely felt implications, not least because ITER is planned to operate with a level of ripple considerably higher than JET. In fact, the European Fusion Development Agreement and Fusion for Energy, the newly formed European

legal entity for ITER, have recently launched a task to investigate ripple losses in ITER, mainly by means of orbit-following simulations, in response to the attention given to ripple losses in recent experimental and modelling work, including the efforts described in this thesis. It should also be noted ELM mitigation is going to be an uncompromisable necessity in future large tokamak reactors, if the H-mode is to remain as an operational scenario. Here, the result that ELM mitigation by magnetic ripple may be a viable scheme is ushered in as a welcome prospect.

Modelling transport phenomena inside the last closed magnetic surface is comparatively straightforward, because here the problem can be reduced to one dimension. To some extent this thesis has also dealt with the inherently even more complex task of modelling transport in the scrape-off layer, i.e. outside the magnetic separatrix, where the problem requires two-dimensional treatment. In particular, the propagation of a heat pulse induced at the outer midplane has been studied with the integrated transport code COCONUT, which couples the 2D edge transport code EDGE2D with the 1.5D core transport code JETTO. In this work, balancing the perpendicular transport across the field lines with the much faster parallel transport along the field lines turned out to be more delicate than expected and still could not reproduce the experimentally observed fluxes at the divertor targets. The analysis has led to the conclusion that fluid approximation alone, which describes the plasma in terms of macroscopic quantities, is insufficient during transients and has to be complemented by the more fundamental kinetic approach, which makes use of a distribution function obtained by solving fundamental equations.

On the whole, the work described in this thesis gives a demonstration of the complex interplay of edge transport phenomena and ELMs in particular with the plasma as a whole and how techniques of various sophistication can be used to study and explain these intricate connections. As has been shown, even crude models can be useful in predictive modelling and contribute to revealing the fundamental dynamics behind intricacies such as the influence of ripple transport on ELM characteristics and plasma performance. Indeed, given that ELMs and similar phenomena are not understood at an in-depth level, present models will without exceptions be simplifications of various degrees, capable at their best to provide qualitative explanations for the effects concerned. Despite having been used very successfully in predictive transport modelling to predict and explain various physics effects, present ELM models lack the true predictive capability of resolving the characteristics of individual ELMs. Even predicting the ELM frequency, let alone the destructiveness of individual ELMs, often proves to be too complex a task even for the most refined and perfected of today's ELM models. Getting there may be a long and arduous path to proceed along, and may perhaps even eventually become a goal of lesser urgency with the development of satisfactory ELM mitigation techniques and ELM-free modes of operation.

Bibliography

[1] J.P. Holdren, Ann. Rev. Energy Environ. **16** 235 (1991).

[2] J. Raeder *et al.*, in Safety and Environmental Assessment of Fusion Power (SEAFP), European Commission, Brussels (1995).

[3] S. Pfalzner, "An Introduction to Inertial Confinement Fusion (Plasma Physics)", CRC Press Taylor & Francis Group, Boca Raton, FL, USA (2006).

[4] W.M. Stacey, "Fusion and Technology: An Introduction to the Physics and Technology of Magnetic Confinement Fusion", John Wiley & Sons Inc. (1984).

[5] B.B. Kadomtsev, "Tokamak Plasma: a Complex Physical System", Institute of Physics Publishing, Bristol, United Kingdom (1992).

[6] J. Wesson: "Tokamaks", 2nd edition, Oxford University Press, Oxford, United Kingdom (1997).

[7] J.D. Lawson, Proc. Phys. Soc. B **70** 6 (1957).

[8] D.R. Sweetman, Nucl. Fusion **13** 157 (1973).

[9] J.G. Cordey, "The neutral injection heating of toroidal plasmas to ignition" in Physics of Plasmas Close to Thermonuclear Conditions, Report EUR FU BRU/XII/476/80, Ed. Commission of the European Communities, Brussels, Belgium, I, 359 (1979).

[10] R.A. Cairns, "Radio-frequency Heating of Plasmas", Institute of Physics Publishing, Bristol, United Kingdom (1991).

[11] N.L. Cardozo, Transactions of Fusion Science and Technology, **45** 321 (2004).

[12] J. Boedo *et al.*, Phys. Rev. Lett **84** 2630 (2000).

[13] P. Helander, D. Sigmar, "Collisional Transport in Magnetized Plasmas", Cambridge University Press, Cambridge, United Kingdom (2002).

[14] T.J.M. Boyd, J.J. Sanderson, "The Physics of Plasmas", Cambridge University Press, Cambridge, United Kingdom (2003).

[15] R. Balesku, "Transport Processes in Plasmas: Neoclassical Transport Theory v. 2", Elsevier Science Ltd (1988).

[16] R. Balesku, "Aspects of Anomalous Transport in Plasmas", Institute of Physics Publishing, Bristol, United Kingdom (2005).

[17] B.B. Kadomtsev, O.P. Pogutse, "Turbulence in Toroidal Systems", Reviews of Plasma Physics, Consultants Bureau, New York, NY, USA **5** 249 (1970).

[18] H. Goedbloed, S. Poedts, "Principles of Magnetohydrodynamics: With Applications to Laboratory and Astrophysical Plasmas", Cambridge University Press, Cambridge, United Kingdom (2004).

[19] G.T.A. Huysmans, "External Resistive Modes in Tokamaks", PhD Thesis, Free University Amsterdam (1991).

[20] H. Goedbloed, Transactions of Fusion Science and Technology, **45** 85 (2004).

[21] F. Wagner *et al.*, Phys. Rev. Lett. **49** 1408 (1982).

[22] B. Coppi, N. Sharky, Nucl. Fusion **21** 1363 (1981).

[23] F. Ryter *et al.*, Phys. Rev. Lett. **86** 2325 (2001).

[24] G.T. Hoang *et al.*, Phys. Rev. Lett. **87** 125001 (2001).

[25] D.R. Baker *et al.*, Phys. Plasmas **8** 4128 (2001).

[26] P. Mantica *et al.*, Plasma Phys. Control. Fusion **44** 2185 (2002).

[27] A.G. Peeters, Nucl. Fusion **42** 1376 (2002).

[28] D.R. Mikkelsen *et al.*, Nucl. Fusion **43** 30 (2003).

[29] X. Garbet *et al.*, Plasma Phys. Control. Fusion **46** 1351 (2004).

[30] H. Zohm, Plasma Phys. Control. Fusion **38** 105 (1996).

[31] C.C. Hegna *et al.*, Phys. Plasmas **3** 584 (1996).

[32] J.W. Connor, Plasma Phys. Control. Fusion **40** 531 (1998).

[33] J.W. Connor *et al.*, Phys. Plasmas **5** 2687 (1998).

[34] G.T.A. Huysmans, T. Hender, B. Alper, Nucl. Fusion **38** 179 (1998).

[35] H.R. Wilson *et al.*, Phys. Plasmas **6** 873 (1999).

[36] B.N. Rogers, J.F. Drake, Phys. Plasmas **6** 2797 (1999).

[37] R.J. Hastie, P.J. Catto, J.J. Ramos, Phys. Plasmas **7** 4561 (2000).

[38] S. Saarelma, Plasma Phys. Control. Fusion **42** A139 (2000).

[39] P.B. Snyder, H.R. Wilson *et al.*, Phys. Plasmas **9** 2037 (2002).

[40] A.V. Chankin, G. Saibene, Plasma Phys. Control. Fusion **41** 913 (1999).

[41] J.W. Connor, Plasma Phys. Control. Fusion **40** 531 (1997).

[42] W. Suttrop, Plasma Phys. Control. Fusion **42** A1 (1999).

[43] ITER Physics Basis Editors *et al.*, "ITER Physics Basis, Chapter 1: Overview and summary", Nucl. Fusion **39** 2137 (1999).

[44] Editors M. Shimada *et al.*, "Progress in the ITER Physics Basis", Nucl. Fusion **47** S01 (2007).

[45] R. Aymar, P. Barabaschi, and Y. Shimomura, Plasma Phys. Control. Fusion **44** 519 (2002).

[46] E. Joffrin, Plasma Phys. Control. Fusion **49** B629 (2007).

[47] P.C. Stangeby: "Plasma Boundary of Magnetic Fusion Devices", Institute of Physics Publishing, Bristol, United Kingdom (2000).

[48] P.N. Yushmanov, Review of Plasma Physics, v. 16, Consultants Bureau, New York, NY, USA (1991).

[49] P.H. Rebut *et al*, Nucl. Fusion **25** 1011 (1985).

[50] Special issue on JT-60U, Fusion Science and Technology **42** 179-584 (2002).

[51] G. Saibene *et al.*, Plasma Phys. Control. Fusion **46** A195 (2004).

[52] V. Parail *et al.*, Proc. 19th IAEA International Conference on Fusion Energy, International Atomic Energy Agency, Vienna, Austria (2002).

[53] J. Lönnroth *et al.*, Contrib. Plasma Phys. 46 249 (2006).

[54] G. Cennachi, A. Taroni, JET Internal Report (88) 03 (1988).

[55] F.L. Hinton, R.D. Hazeltine, Rev. Mod. Phys. **48** 239 (1976).

[56] L. Lao, Nucl. Fusion **25** 1421 (1985).

[57] J.M. Rawls, M.S. Chu, F.L. Hinton, Phys. Fluids **18** 1160 (1975).

[58] B.D. Scott, Plasma Phys. Control. Fusion **49** S25 (2007).

[59] V. Parail *et al.*, Nucl. Fusion **39** 429 (1999).

[60] M. Erba *et al.*, Plasma Phys. Control. Fusion **39** 261 (1997).

[61] A Taroni *et al.*, Plasma Phys. Control. Fusion **36** 1629 (1994).

[62] W.A. Houlberg *et al.*, Phys. Plasmas **4** 3231 (1997).

[63] P. Snyder *et al.*, Proc. 22nd IAEA Fusion Energy Conference (2008).

[64] C.D. Challis *et al.*, Nucl. Fusion **29** 563 (1989).

[65] M. Bornatici *et al.*, Nucl. Fusion **23** 1153 (1983).

[66] V. Erckmann, U. Gasparino, Plasma Phys. Control. Fusion **36** 1869 (2004).

[67] R. Prater, Phys. Plasmas **11** 2349 (2004).

[68] S. Tamor, J. Comput. Phys. **40** 104 (1981).

[69] J.M. Hammersley, D.C. Handscomb, "Monte Carlo Methods", Chapman and Hall, London, United Kingdom and New York, NY, USA (1964).

[70] L. Devroye, "Non-Uniform Random Variate Generation", Springer-Verlag, Berlin, Germany, Heidelberg, Germany and New York, NY, USA (1986).

[71] JET Team (presented by A. Taroni), Proc. 16th IAEA International Conference on Fusion Energy, Volume 2, p. 477 (1996).

[72] R. Simonini, Contrib. Plasma Phys. **34** 368 (1994).

[73] R. Schneider *et al.*, Contrib. Plasma Phys. **46** 3 (2006).

[74] G.J. Radford "Classical parallel transport in a multi-species plasma from a 21 moment approximation", JET Report JET-R(93)05 (1993).

[75] E. Cupini, A. de Matteis, R. Simonini, NET Report no 9, EUR XII-324/9, Commission of the European Communities, Brussels, Belgium (1983).

[76] D. Reiter, "The EIRENE code, Version Jan. 92, User Manual", Forschungszentrum Jülich, Germany (1992).

[77] T. Kurki-Suonio *et al.*, Nucl. Fusion **42** 725 (2002).

[78] J.A. Heikkinen *et al.*, J. Comput. Phys. **173** 527 (2001).

[79] G.T.A. Huysmans, J.P. Goedbloed, W. Kerner, "Isoparametric bicubic Hermite elements for solution of the Grad-Shafranov equation", Proc. Europhysics 2nd Intern. Conf. on Computational Physics 1990, World Scientific 371 (1991).

[80] A.B. Mikhailovskii *et al.*, Plasma Phys. Rep. **23** 844 (1997).

[81] G. Saibene *et al.*, Proc. 28th EPS Conference on Plasma Physics and Controlled Fusion (2001).

[82] J. Stober *et al.* Nucl. Fusion **41** 1123 (2001).

[83] O. Gruber *et al.*, Proc. 19th IAEA Conference, Lyon, France (2002).

[84] Y. Kamada *et al.* Plasma Phys. Control. Fusion **44** A279 (2002).

[85] Y. Kamada *et al.*, Plasma Phys. Control. Fusion **42** A247 (2000).

[86] L. Lao *et al.* Nucl. Fusion **41** 295 (2001).

[87] B. Coppi *et al.* Nucl. Fusion **19** 715 (1979).

[88] G.T.A. Huysmans, S.E. Sharapov, A.B. Mikhailovskii, W. Kerner, Phys. Plasmas **8** 4292 (2001).

[89] J. Weiland, "Collective Modes in Inhomogeneous Plasmas", Institute of Physics Publishing, Bristol, United Kingdom (2000).

[90] C. Mercier, Nucl. Fusion **1** 47 (1960).

[91] C. Mercier, Nucl. Fusion Suppl. **2** 801 (1962).

[92] ITER Physics Expert Group on Confinement *et al.*, "ITER Physics Basis, Chapter 2: Plasma confinement and transport", Nucl. Fusion **39** 2175 (1999).

[93] J.G. Cordey, Nucl. Fusion **43** 670 (2003).

[94] D. McDonald *et al.*, Nucl. Fusion **47** 147 (2007).

[95] K. Burrell *et al.*, Proc. 22nd IAEA Fusion Energy Conference (2008).

[96] T.P. Kiviniemi *et al.*, Proc. 32nd European Physical Society Conference on Plasma Physics (2005).

[97] B. Tubbing, Proc. 22nd European Physical Society Conference on Controlled Fusion and Plasma Physics, Europhysics Conference Abstracts, Vol 19C, part IV, p. IV-001 (1995).

[98] V. Parail *et al.*, Proc. 21nd IAEA Fusion Energy Conference (2006).

[99] T. Eich *et al.*, J. Nucl. Mat. **363-365** 989 (2007).

[100] D. Tskhakaya *et al.*, Contrib. Plasma Phys. **48** 89 (2008).

[101] E.R. Solano, Plasma Phys. Control. Fusion **46** L7 (2004).

[102] E.R. Solano *et al*, Nucl. Fusion **48** 065005 (2008).

Appendices

Publications 1 – 6

ISBN 978-952-248-157-3
ISBN 978-952-248-158-0 (PDF)
ISSN 1795-2239
ISSN 1795-4584 (PDF)